J. Fluid Mech. (1999), *vol.* 382, *pp.* 195–243. Printed in the United Kingdom

Helical vortices in swirl flow

By S. V. ALEKSEENKO, P. A. KUIBIN, V. L. OKULOV AND S. I. SHTORK

Institute of Thermophysics, Novosibirsk 630090, Russia

(Received 20 March 1997 and in revised form 12 August 1998)

Helical vortices in swirl flow are studied theoretically and experimentally.

A theory of helical vortices has been developed. It includes the following results: an analytical solution describing an elementary helical vortex structure – an infinitely thin filament; a solution for axisymmetrical vortices accounting for the helical shape of vortex lines and different laws of vorticity distribution; a formula for calculation of the self-induced velocity of helical vortex rotation (precession) in a cylindrical tube; an explanation of the zone with reverse flow (recirculation zone) arising in swirl flows; and the classification of vortex structures.

The experimental study of helical vortices was carried out in a vertical hydrodynamical vortex chamber with a tangential supply of liquid through turning nozzles. Various vortex structures were formed owing to changing boundary conditions on the bottom and at the exit section of the chamber. The hypothesis of helical symmetry is confirmed for various types of swirl flow. The stationary helical vortex structures are described (most of them for the first time) the features of which agree with the results and predictions of the theoretical model developed. They are the following: a rectilinear vortex; a composite columnar vortex; helical vortices screwed on the right or on the left; a vortex with changing helical symmetry; a double helix – two entangled vortex filaments of the same sign.

1. Introduction

Numerous facts confirm that concentrated vortices of helical shape are widespread in swirl flows (see, for example Saffman 1992). The efficiency of many technological devices with swirl flow depends on the generation of helical vortices arising downstream of the point of columnar vortex breakdown (Gupta, Lilley & Syred 1984). However, most researchers ignore the complex structure of swirl flow in vortex apparatuses. According to the review by Alekseenko & Okulov (1996) only some authors (see Guarga *et al.* 1985; Ishizuka 1989; Kumar & Conover 1993; Yazdabadi, Griffiths & Syred 1994; Bandyopadhyay & Gad-el-Hak 1996) point to the helical structure of the vortex in technological devices with intensive swirling. The helical vortex structures are often mentioned when the phenomenon of vortex breakdown is studied (Chanaud 1965; Sarpkaya 1971; Faler & Leibovich 1977; Escudier 1988; Brücker & Althaus 1992, etc.) However, they were not the main subject of research in those works but only mentioned as being a result of the vortex breakdown. A special experimental study of various large-scale helical vortex structures in a vortex chamber was started in Alekseenko & Shtork (1992).

The main goal of this work is the theoretical and experimental investigation of steady (immobile or rotating with a constant angular velocity) helical vortex structures

in a swirl flow. Simple theoretical models of flow are put forward based on a hypothesis about the helical symmetry of the vorticity field and taking into account the presence of a solid wall (bounded swirl flows). Note that just bounded flows are the subject of study, as it is only on account of the wall's influence that we are able to explain a number of phenomena arising in vortex chambers. As a result of the investigation a classification is made of helical vortex structures generated in swirl flows.

In the next section the experimental set-up and methods of studying swirl flow are described. Similarly to the case of a vortex breakdown (Faler & Leibovich 1977) it has been established that the commonly used parameters of swirl flow (Reynolds and swirl numbers) do not uniquely characterize the flow structure.

The third section is devoted to the theoretical description of flows with helical symmetry. The assumption about helical symmetry results in an important simplification of the mathematical problem. Earlier attempts were undertaken to construct simple models for a flow with helical symmetry (see, for example, Dritschel 1991 and references therein). However, as a rule the Beltrami condition was used for additional simplification, which assumes identical fields of velocity and vorticity within a constant factor in the whole area of flow. The concentrated vortices do not belong to this class. In our work another class of flows covering the concentrated helical vortices is investigated. A simplifying condition for such flows has been formulated for the velocity components and is valid in the whole area of the flow, unlike the preceding works (Hardin 1982; Okulov 1993, 1995), where the condition of helical symmetry was applied to a vortex filament. The advantage is that the velocity components can be easily checked in an experiment. Hardin (1982) obtained an analytical solution in the form of infinite series of modified cylindrical functions and their derivatives for a helical filament in an unbounded space. A similar representation of the solution was obtained by Okulov (1993, 1995) with a helical filament in a bounded space (cylindrical tube); then it was used for the description of combustion (Borissov, Kuibin & Okulov 1993) and energy separation (Borissov, Kuibin & Okulov 1994) in swirl flow. Both solutions have a fairly complex form, which is unsuitable for flow analysis. Besides, the series involved in these solutions diverge at the points of the vortex filament. For correct computation of the velocity field and the stream function it is appropriate to separate the singularities from the solution in explicit form. Such a procedure for both the stream function and the velocity is carried out here. As a result, flows induced by both the left-handed and right-handed helical filaments with different parameters are analysed. The difference between the left- and right-handed geometry of a vortex was revealed by Fukumoto & Miyazaki (1991) for the stability characteristics in a second-order cut-off model. A new fact established in the present work is that the origin of reverse flow in a central zone of swirl flow is possible only for left-handed vortices.

We cannot describe all the properties of swirl flows with the help of an elementary vortex structure – an infinitely thin helical filament – as real vortices have a finite core size. In § 4 we start to consider this class of helical vortices with the simplest particular case of axisymmetrical or columnar vortices. Elementary models of such vortices have long been in existence: Rankine, Lamb, Burgers etc. (Hopfinger & van Heijst 1993). However, the above models yield only the radial distribution of the tangential component of a velocity vector. The axial component does not depend on the radius, which is inconsistent with the numerous experimental data. We propose a model of an axisymmetrical vortex as a superposition of the helical vortex filaments with a profile of the axial velocity that matches the experimental data well. In the experiment we also obtained a more complex axisymmetrical vortex structure with an

inner core consisting of left-handed helical filaments encircled by an annular vortex consisting of right-handed ones.

The motion of a helical vortex is of great interest. It is known that a helical vortex filament is a representative of a class of filaments which move without changing form, with constant velocities of rotational and translational motions (Kida 1981). Many works are devoted to determining the velocity of the self-induced motion of helical vortex filaments in an unbounded space (Joukowski 1912; Crow 1970; Widnall 1972; Widnall & Bliss 1971, etc.). An important result found by Kelvin (1880) was the determination of the rotational velocity of a weakly curved columnar vortex. Moore & Saffman (1972) derived a generalized formula which accounted for details of the vorticity distribution inside the vortex core. Later their result was confirmed in experiments by Maxworthy, Hopfinger & Redekopp (1985). A vortex with a small helical pitch was considered by Levy & Forsdyke (1928). A full comparison of these investigations was performed by Ricca (1994). In § 5 the influence of a solid wall on the rotation of the helical vortex filament is estimated. Hashimoto (1971) tried to determine the wall effect, neglecting the self-induced velocity related to the curvature and torsion of a filament. But his result is devalued by errors, even for the velocity induced by the wall. Kuibin & Okulov (1994) obtained a formula for the rotation frequency in a cylindrical tube. However, they used a fairly rough approach for the estimation of the self-induced velocity. Using Ricca's (1994) prescription of Kelvin's (1880) formula we succeeded in making quite a precise evaluation of the contribution of different effects to vortex motion in a tube.

As a result, the existence of immobile helical vortex structures in bounded space has been predicted. The velocity of their self-induced motion is compensated by the wall's effect and translational flow along an axis. The last section is devoted to the description of the experimental investigation of such vortex structures. We detected the following immobile structures: a right-handed vortex, a left-handed vortex, a vortex with a change of helical symmetry; and a double helix – two intertwisted vortex filaments of the same sign.

2. Experimental methods

2.1. *Experimental equipment*

It is most convenient to study helical vortices in vortex chambers with controlled geometric and regime parameters. Our experimental investigations of concentrated vortices were performed in the tangential chamber shown in figure 1. The test section, made of Plexiglas, was a vertical chamber of a square cross-section with dimensions of $188 \times 188 \times 600$ mm. Straight-flow rectangular nozzles with an outlet section of 23×14 mm (the former is the vertical size) were mounted at three levels and aggregated in corner units, 15 mm from the chamber corner. The turning angle of each nozzle may be changed in the range of $\gamma = 0$–40°.

The swirling flow was generated by directing the nozzle at a tangent to a certain circumference of diameter d with its centre on the channel axis. It is known (Escudier, Bornstein & Zehnder 1980; Gupta *et al.* 1984) that the conditions at the outlet and closed endwall of a chamber have the most significant influence on the flow structure in cyclone-vortex chambers. In particular, a concentrated vortex like a vortex filament is observed in a chamber with a diaphragmed outlet. The geometric conditions in the tangential chamber were varied by changing the nozzle direction and bottom shape, diaphragming the outlet, and displacing the outlet orifice.

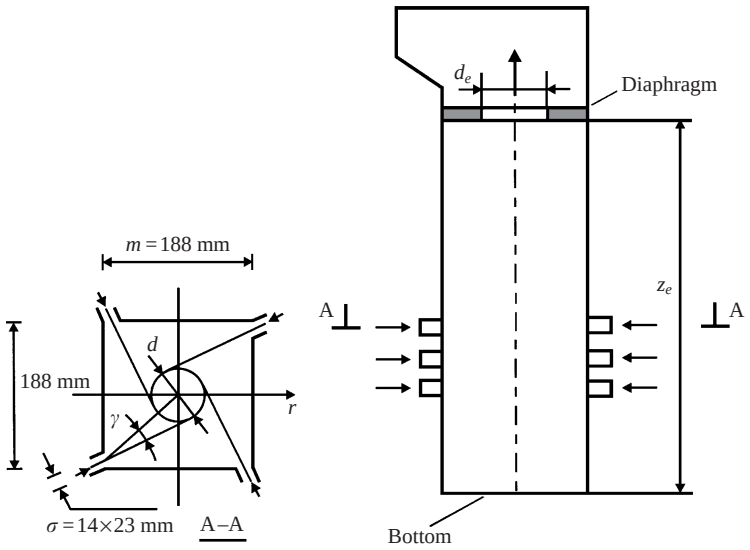

FIGURE 1. Schematic diagram of the vortex chamber with a tangential supply of liquid. The chamber has 12 rectangular nozzles with variable turning angle γ. d is the diameter of the conventional circumference.

The vortex chamber used in the experiment is not canonical due to the square form of its cross-section. Nonetheless, it was the most suitable for studying a variety of vortex structures. Moreover it was shown with the help of cylindrical inserts that, for regimes with concentrated vortices, the flow patterns in near-axis areas of cylindrical and rectangular channels practically do not differ from each other. This fact may be explained by the existence of corner vortices that induce an imaginary near-cylindrical surface inside which a flow induced by the main vortex develops.

Water was used as the working liquid. The flow visualization was made possible with tiny air bubbles. In the experiments, the distributions of velocity and static pressure were measured. To measure the wall pressure, holes with a diameter of 0.4 mm were used. Static pressure in the flow was determined by a Pitot-static tube with a diameter of 1.4 mm. The pressure value was measured with a resistance strain transducer.

The profiles of tangential and axial components of velocity were measured using three methods: standard drop tubes with a diameter of 1.4 mm (far from the vortex axis), stroboscopic particle visualization (Shtork 1994) and the electrodiffusion method (Alekseenko & Shtork 1992).

2.2. *Parameters of swirl flow*

As for any viscous flow, the basic regime parameter of flow in a vortex chamber is the Reynolds number $Re = Q/(mv)$, where Q is the flow rate, m is the chamber width, and v is the kinematic viscosity. To characterize the degree of flow swirling in a vortex chamber, a swirl number S is introduced. Various ways of determining this parameter exist. The simplest expressions represent the ratios of maximum tangential velocity to a maximum axial one, or the averaged tangential velocity to an averaged axial one. The most widespread definition is (Gupta *et al.* 1984)

$$S = F_{mm}/F_m L_S. \tag{2.1}$$

Here $F_{mm} = \int_\Sigma \rho w_\varphi w_z r \, \mathrm{d}\Sigma$ is the axial component of the angular momentum flux, $F_m = \int_\Sigma (p + \rho w_z^2)\mathrm{d}\Sigma$, is the axial component of the momentum flux, w_z and w_φ are the axial and tangential velocity components, r is the radial coordinate, ρ is the fluid density, L_S is the characteristic size (radius in the case of a cylindrical chamber), p is the superatmospheric pressure, Σ is the cross-section area. The turbulent fluctuations are generally neglected, therefore the pressure and velocities are considered to be time-averaged.

An exact calculation of the swirl number by formula (2.1) is practically impossible since the velocity and pressure fields are usually unknown. However, one can evaluate a swirl number through the geometric parameters of a chamber. Let us estimate the swirl number for the tangential chamber shown in figure 1.

The axial component of the angular momentum flux (for the same nozzle velocities and diameter d) may be approximately written as

$$F_{mm} = \sum_{i=1}^{n} (G'V'd/2)_i = GV'd/2 = G^2 d/2\rho\Sigma'.$$

Here i is the nozzle number, n is the number of nozzles, G is the total mass flow rate, G' is the mass flow rate through the nozzle, V' is the mean velocity at the nozzle exit section weighted by the momentum, Σ' is the cross-section area of all the nozzles.

The momentum flux is, correspondingly, expressed by the formula $F_m = GV = G^2/\rho\Sigma$, where V is the velocity in the chamber cross-section area weighted by the momentum. It follows from (2.1) that $S = \Sigma\, d/(2\Sigma' L_S)$. Assuming that $\Sigma = m^2$, $L_S = m/2$, $\Sigma' = n\sigma$, where σ is the cross-section area of one nozzle, the swirl number can be finally estimated as

$$S = md/(n\sigma). \tag{2.2}$$

As is seen, parameter S depends only on the geometrical characteristics of the device, therefore it is called the design swirl number. In Feikema, Chen & Driscoll (1990) a direct comparison of the geometrical swirl parameter with its precise value obtained by (2.1) was performed for a channel with axial symmetry. Despite the quantitative differences a good correlation was observed between these definitions.

However, further numerous experimental investigations of swirl flows (Alekseenko & Shtork 1992; Alekseenko *et al.* 1994) showed that the Reynolds number and swirl number did not uniquely characterize the flow regime. In particular, the conditions at the exit and the bottom of a chamber play an essential role. Quite different flow structures, which will be described in §§ 4 and 6, were observed in the vortex chamber at approximately the same values of flow rate Q and swirl number S but for different conditions at the chamber endwalls: a rectilinear vortex (flat bottom and a diaphragmed outlet with a central orifice); a precessing vortex (flat bottom and open outlet in the chamber); a left-handed helical vortex (flat bottom and a displaced outlet orifice); a double helix – two entangled vortices (two flat slopes on the bottom and a central outlet orifice). In all cases the direction of the flow swirl was the same.

Two important points follow from the observations: (i) Re and swirl number S do not uniquely characterize the flow structure; (ii) the observed vortex structures have helical symmetry which means the existence of a spatial period along the z-axis. The former point is accepted as the main assumption in the theoretical model of helical vortices.

3. Two-dimensional flow with helical symmetry

3.1. *Governing equations*

Let us consider the swirl flow of an inviscid incompressible fluid in a cylindrical channel of radius R. The right-handed system of cylindrical coordinates is used with radius-vector $\boldsymbol{r} = (r, \varphi, z)$ and axis z coinciding with the tube axis. The coordinate system is chosen so that the direction of flow swirl agrees with the positive direction of angle φ. The directions of the stream and axis z may not coincide. It is assumed that the swirl flow has *helical symmetry* (see Landman 1990; Dritschel 1991). This means that the flow characteristics conserve their values along the helical lines given by the equations: $r = \text{const}$ and $\varphi - z/l = \text{const}$ with the tangent vector $\boldsymbol{B} = B^2[\boldsymbol{e}_z + (r/l)\,\boldsymbol{e}_\varphi]$. $\boldsymbol{B}$ is referred to as the 'Beltrami vector'. Here $B^2 = (1 + r^2/l^2)^{-1}$, $h = 2\pi l$ is the pitch of the helical symmetry, $\boldsymbol{e}_z$ and $\boldsymbol{e}_\varphi$ are the axial and circumferential unit vectors respectively. The quantity l has a positive value for right-hand helical symmetry and a negative value for the left-hand one. $\boldsymbol{B}$ is orthogonal to the radial unit vector $\boldsymbol{e}_r$. The cross-product of $\boldsymbol{B}$ with $\boldsymbol{e}_r$ defines a third orthogonal vector in the direction $\varphi - z/l$: $\boldsymbol{\chi} = \boldsymbol{B} \times \boldsymbol{e}_r = B^2[\boldsymbol{e}_\varphi - (r/l)\,\boldsymbol{e}_z]$. Now, let us introduce quantities associated with projections of the velocity vector $\boldsymbol{w} = (w_r, w_\varphi, w_z)$ on $\boldsymbol{B}$ and $\boldsymbol{\chi}$:

$$w_B = \frac{\boldsymbol{B}\cdot\boldsymbol{w}}{B^2} = w_z + \frac{r}{l}\,w_\varphi\,, \qquad w_\chi = \frac{\boldsymbol{\chi}\cdot\boldsymbol{w}}{B^2} = w_\varphi - \frac{r}{l}\,w_z, \tag{3.1}$$

and write the continuity and Euler equations with the use of (3.1):

$$\frac{\partial (r w_r)}{\partial r} + \frac{\partial w_\chi}{\partial \chi} = 0, \tag{3.2}$$

$$\frac{\partial w_r}{\partial t} + w_r\frac{\partial w_r}{\partial r} + w_\chi\frac{\partial w_r}{r\partial \chi} - \frac{B^4}{r}\left(w_\chi + \frac{r}{l}w_B\right)^2 = -\frac{1}{\rho}\frac{\partial p}{\partial r}, \tag{3.3}$$

$$\frac{\partial w_\chi}{\partial t} + w_r\frac{\partial w_\chi}{\partial r} + w_\chi\frac{\partial w_r}{r\partial \chi} - B^2 w_r\left(2\,\frac{r}{l}\,w_B + (2 - B^{-2})w_\chi\right) = -\frac{B^{-2}}{\rho}\frac{\partial p}{r\partial \chi}, \tag{3.4}$$

$$\frac{\partial w_B}{\partial t} + w_r\frac{\partial w_B}{\partial r} + w_\chi\frac{\partial w_B}{r\partial \chi} = 0. \tag{3.5}$$

The continuity equation in helical variables (3.2) permits the following decomposition of the velocity field (Landman 1990):

$$\boldsymbol{w} = w_B\boldsymbol{B} + \nabla\Psi \times \boldsymbol{B}. \tag{3.6}$$

The same form of decomposition is valid for the vorticity field also:

$$\boldsymbol{\omega} = \zeta\,\boldsymbol{B} + \nabla v \times \boldsymbol{B}. \tag{3.7}$$

The four scalar functions on the right-hand side of (3.6) and (3.7) are functions of (r, χ, t). The kinematic condition $\boldsymbol{\omega} = \nabla \times \boldsymbol{w}$ implies that

$$v = w_B\,, \qquad \Delta^*\,\Psi = 2B^4 w_B/l - B^2\zeta, \tag{3.8}$$

where

$$\Delta^* \equiv \frac{1}{r}\frac{\partial}{\partial\, r}\left(rB^2\frac{\partial}{\partial\, r}\right) + \frac{1}{r^2}\frac{\partial^2}{\partial\,\chi^2}$$

is the helical Laplacian operator.

Further, we shall restrict our consideration to a class of flows in which the equation (3.5) is satisfied identically. The simplest solution of this equation is $w_B = \text{const}$. In

this case the flow is two-dimensional. The constant corresponds to the value of the axial velocity w_0 at $r = 0$ determining a uniform flow imposed on a basic one, i.e.

$$w_z = w_0 - \frac{r}{l} w_\varphi \qquad \text{or} \qquad \frac{w_z - w_0}{w_\varphi} = -\frac{r}{l}. \tag{3.9}$$

On the other hand this condition together with (3.8) and (3.7) means both that a vorticity vector is directed along the helical line:

$$\boldsymbol{\omega} = \zeta \boldsymbol{B} = \left(0,\ B^2 \zeta\, r/l,\ B^2 \zeta\right), \tag{3.10}$$

and that velocity and vorticity fields are orthogonal in a frame of reference moving with velocity w_0 along axis z, unlike the helical Beltrami flows, where they are parallel to each other (Dritschel 1991). As the velocity field is now presented by the single function

$$\boldsymbol{w} = \left(\frac{1}{r}\frac{\partial \Psi}{\partial \chi},\quad B^2\left(w_0 \frac{r}{l} - \frac{\partial \Psi}{\partial r}\right),\quad B^2\left(w_0 + \frac{r}{l}\frac{\partial \Psi}{\partial r}\right)\right), \tag{3.11}$$

Ψ may be called a stream function.

To close the problem we have to derive an equation for function ζ (or ω_z). The Helmholtz equation for the axial component of vorticity in the helical variables reads

$$\frac{\partial \omega_z}{\partial t} + w_r \frac{\partial \omega_z}{\partial r} + w_\chi \frac{\partial \omega_z}{r \partial \chi} = \omega_r \frac{\partial w_z}{\partial r} + \left(\omega_\varphi - \frac{r}{l}\,\omega_z\right)\frac{\partial w_z}{r \partial \chi}. \tag{3.12}$$

In view of (3.10) the right-hand side of (3.12) equals zero. This means that ω_z does not vary along the trajectory of a liquid particle, and in the stationary case ω_z is an arbitrary function of stream function Ψ.

Further, it is assumed that the distribution of vorticity $\boldsymbol{\omega}$ is a known vector-function of coordinates satisfying relations (3.10), (3.12) and the problem is reduced to the solution of a linear differential equation for the stream function Ψ:

$$\Delta^* \Psi = 2B^4 w_0/l - \omega_z \tag{3.13}$$

with the boundary condition at the wall

$$w_r|_{r=R} = r^{-1}\, \partial \Psi / \partial \chi|_{r=R} = 0. \tag{3.14}$$

Helix pitch l and velocity w_0 at the flow axis are the parameters of the problem.

The problem of reconstructing a velocity field using the given vorticity distribution in the case of an unbounded space is usually solved on the basis of an integral representation of the solution in the form of the Biot-Savart law. In practical applications, however, the case of bounded flows is more important. With a solid boundary, the Biot-Savart law is of little use since the vorticity distribution at the wall is unknown. In this connection the solving of the linear problem (3.13)–(3.14) looks to be a more promising way.

3.2. *Novel local integral characteristics; testing helical symmetry*

As is shown in § 2.2, the swirl number S and flow rate Q (or Re in the case of viscous fluid) do not unequivocally determine the structure of the swirl flow in a vortex chamber. An alternative approach for flows with helical symmetry is related to introducing two novel parameters. They follow from the above theoretical analysis and are the helix pitch, $2\pi l$, and the velocity of uniform flow, w_0. These parameters are involved in (3.9) connecting the axial and tangential components of velocity in a two-dimensional helical flow.

In the particular case of zero axial velocity, helix pitch l is uniquely determined through the integral swirl parameter S. Actually, one can obtain l from (3.9) by multiplying it by w_z, integrating over the cross-section of the flow at $w_0 = 0$, and allowing for (2.1):

$$l = -F_{mm}/F_m = -L_S S\,.$$

Here the pressure contribution is excluded from the definition of the momentum flux $F_m = \rho \int w_z^2\, r\, \mathrm{d}r\, \mathrm{d}\varphi$ in accordance with a definition by Feikema *et al.* (1990).

If the axial velocity at the symmetry axis of the flow is not equal to zero, which most often occurs in experiments, then we have from (3.9):

$$l = -F_{mm}/(F_m - w_0\, G) = -L_S S/(1 - w_0\, G/F_m), \tag{3.15}$$

where G is the mass flow rate. Thus, in arbitrary swirling flow with helical symmetry, the helix pitch depends not only on the swirl number S but also on the value of the velocity at the axis w_0 determining uniform flow.

It should be noted, however, that in actual flow, as a rule, the condition of helical symmetry is not satisfied along the entire length of the experimental set-up. The flow undergoes several transformations with distance from the swirling arrangement – from vortex breakdown to complete decay of the swirl. The assumption of helical symmetry in the proposed model means an identical flow structure with the period of $2\pi l$ along the z-axis for an infinitely long interval. It is clear that such an assumption is not suited to the whole flow region. Nonetheless many authors (Leibovich 1984; Escudier 1988 etc.) show that fairly long regions exist in a swirl flow where the velocity profiles vary only moderately. It would be reasonable to apply a hypothesis of helical symmetry to these regions in a local sense. To do this we should test condition (3.9) for real swirl flow. If such an approach is valid then parameters l and w_0 may be accepted as the new swirl flow characteristics.

To verify the hypothesis of helical symmetry we shall compare the measured values of axial velocity with the values calculated by formula (3.9) through measured values of tangential velocity at the same points. Initially it is necessary to determine parameters l and w_0. If the local flow characteristic w_0 is measured directly in a given cross-section the value of l may be computed immediately from (3.15). However, it is not always possible to do this with sufficient accuracy since detailed data on velocity fields are usually unknown. The problem of determining l may be simplified significantly if the linear relation between the velocity components in (3.9) is taken into account. After averaging (3.9) the simple formula

$$l = \langle r w_\varphi \rangle / \big(w_0 - \langle w_z \rangle\big) \tag{3.16}$$

follows where angle brackets mean averaging. The averaging in (3.16) may be done over either whole cross-sections of the tube or some parts where helical symmetry exists. In particular, the vicinity of the tube wall, where viscous effects occur, was excluded during the processing of experimental data. The comparison of results of averaging with different weight functions shows that in the case of a small number of measurement points on the radial coordinate averaging over the cross-section with weight function $1/r$ is the best.

Generally, the value of the velocity at the flow axis is unknown or is determined with large error. Then parameters l and w_0 are found by minimizing the mean-square deviation from zero of the functional

$$\Big\langle \big(l w_z - l w_0 + r w_\varphi\big)^2 \Big\rangle.$$

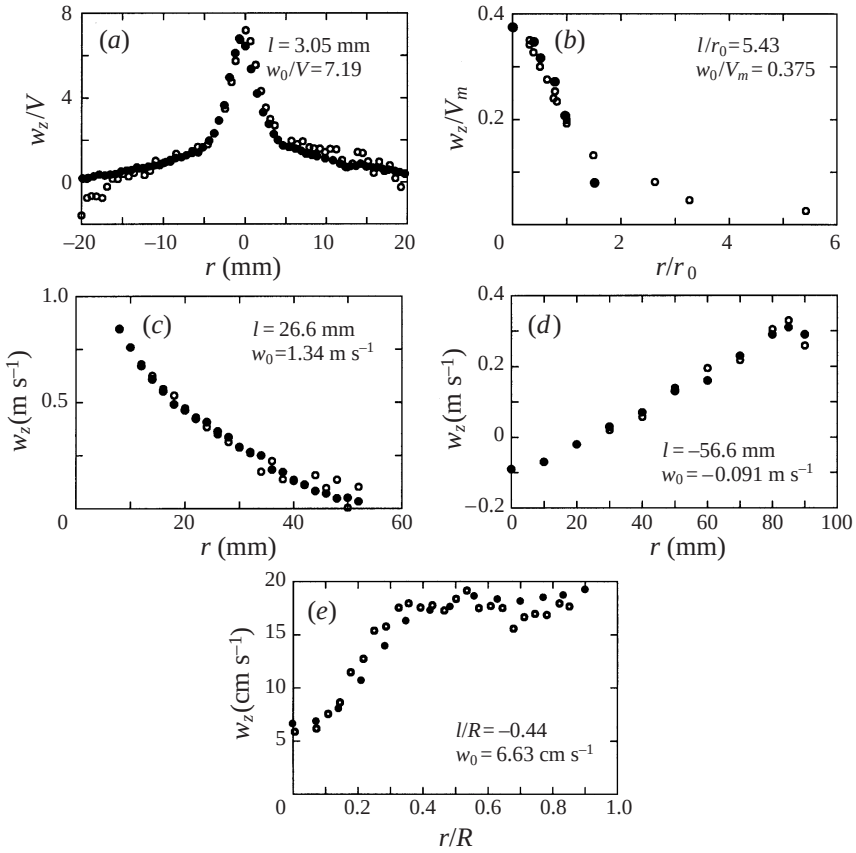

FIGURE 2. Testing of the local helical symmetry in swirl flows with different types of tangential swirl generators. (*a*) Slit swirler (Escudier 1988, class A, cross-section iii, V is the velocity in the inlet slit); (*b*) rotating tank with a central suction tube (Maxworthy, Hopfinger & Redekopp 1985, $\Omega = 1.51$ s^{-1}, $Q = 180$ l h^{-1}); nozzle swirler (Shtork 1994), (*c*) diaphragmed exit orifice, $d_e = 70$ mm, $z_e = 430$ mm, $Re = 2.8 \times 10^4$, $S = 3$, $z = 323$ mm, (*d*) chamber without a diaphragm, $Re = 3.2 \times 10^4$, $S = 1$, $z = 385$ mm; (*e*) vane swirler (Garg & Leibovich 1979, $Re = 11480$, swirl parameter, $\Omega = 0.79$, $z = 19.3$ cm, R is the chamber radius). (*a–c*) Stationary swirl flow, (*d,e*) swirl flows with a precessing vortex core. ●, Measured values of the axial velocity w_z; ○, axial velocity calculated according to (3.9); l and w_0 are the values of the helix pitch and axial velocity at the axis, r is the radial coordinate.

Substituting the expression for w_0 from (3.16) into this functional we have

$$l = \big(\langle rw_\varphi\rangle\langle w_z\rangle - \langle rw_\varphi w_z\rangle\big)/\big(\langle w_z^2\rangle - \langle w_z\rangle^2\big). \tag{3.17}$$

After computing l by (3.17) we find $w_0 = \langle w_z\rangle - \langle rw_\varphi\rangle/l$.

The testing for local helical symmetry in swirl flows was carried out using various types of swirlers, flow regimes and methods of flow diagnostics described previously. The parameters of helical symmetry l and w_0 were determined with one of the above-described ways. Figure 2 shows comparisons of measured values of axial velocity with the values calculated by formula (3.9) through the measured values of tangential velocity. Solid and open circles represented the measured and calculated values of w_z respectively. The experimental data for flows with straight vortices are presented in figure 2(*a,b,c*). For the case 2(*b*) we can compare the value of pitch found by (3.16), $h = 34.1\, r_0 = 11.2$ cm, with the wavelength measured in experiment by Maxworthy

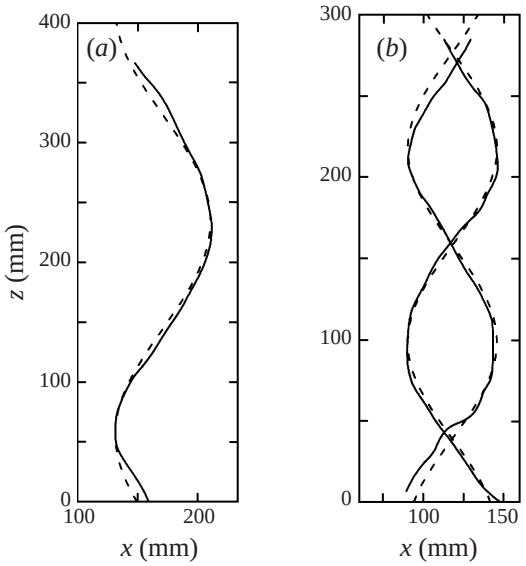

FIGURE 3. Testing of the helical symmetry by comparing the vortex shape with a helix: (*a*) left-handed vortex, (*b*) double helix; ——, the projection of the vortex axis on the vertical plane; - - -, the sinus with parameters: (*a*) $l = 56.5$ mm, $a = 39.5$ mm, (*b*) $l = 37.9$ mm, $a = 27.8$ mm.

et al. (1985), $\lambda = 10.8$ cm. Figure 2(*d*,*e*) shows the data for non-stationary swirl flows where a pronounced precessing vortex core was observed. In the last case the averaging in formulae (3.16) and (3.17) was carried out over time also. It follows from the analysis of the data presented that the helical symmetry is realized in almost all flow regions except the vicinity of the tube wall. In the wall region, such effects appear as the boundary layer (due to the action of viscosity) and Görtler vortices (in the case of a concave wall). Similar conclusions follow from the analysis of experimental data obtained by Faler & Leibovich (1977), Kutateladze, Volchkov & Terekhov (1987) and Guarga *et al.* (1985).

Otherwise the testing of helical symmetry may be done by estimating the quality of the helical shape of the observed vortex structures (see photos in § 6). Such a procedure was followed for the two regimes with pronounced helix-like vortex structures (figures 3*a* and 3*b*). The testing is as follows: the projection of the helix on a plane must be a sinus. To obtain projections of the experimentally observed helical structures, computer processing of the instantaneous video images of the air core, visualizing the vortex axis, was done. The positions of vortex axis projections for single and double vortices are compared with a sinus. Excellent correlation is found. Using these pictures one can easily determine the pitch of helical symmetry. It is different for each depicted vortex: $h = 355$ mm ($l = 56.5$ mm) in figure 3(*a*) and $h = 238$ mm ($l = 37.9$ mm) in figure 3(*b*).

One further important conclusion may be drawn from the analysis of parameters l and w_0 for flow regimes with identical values of swirl parameters and flow rate. The values of the parameters of helical symmetry (see figures 2*c*,*d*; 3*a*,*b*) are quite different for each pattern of swirl flow. For this reason the use of l and w_0 as the main characteristics of swirl flow is confirmed.

The analysis performed points to the existence of helical symmetry in swirl flows

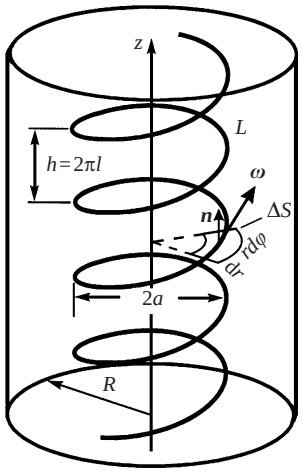

FIGURE 4. Helical vortex filament in a cylindrical tube of radius R; ΔS is the element of the tube cross-section across which the vortex filament passes.

for all types of swirlers and the possibility of describing swirl flows with an inviscid fluid model.

3.3. *Stream function and velocity field for an infinitely thin helical vortex filament in a cylindrical tube*

Let us consider a flow with an infinitely thin vortex filament twisted round an imaginary cylinder of radius a (figure 4). This elementary vortex structure, like a rectilinear vortex filament and a vortex ring, is the fundamental object in the theory of vortex flows.

Initially we should refine the right-hand side of (3.13). For a vortex filament, the vorticity is concentrated along the line L which represents the axis of a helical vortex filament with a pitch of $2\pi l$ twisted round a cylinder of radius a. The circulation Γ, being the strength of the vortex filament, is a constant in this case and is connected to the vorticity by Stokes formula: $\int_{\Delta S} \boldsymbol{\omega} \cdot \boldsymbol{n}\, \mathrm{d}s = \Gamma = \text{const}$. Here ΔS is the surface element across which the vortex filament passes, $\boldsymbol{n}$ is the unit normal vector to this surface. Since only a single z-component of vorticity is included in (3.13), we choose ΔS as the surface element with its normal vector coinciding with the z-axis (see figure 4). Then we have $\int_{\Delta S} \boldsymbol{\omega} \cdot \boldsymbol{n}\, \mathrm{d}s = \int_{\Delta S} \omega_z\, \mathrm{d}s = \int_{\Delta S} \omega_z\, r\, \mathrm{d}r\, \mathrm{d}\varphi$. If variables (r, χ) are used the following equation may be obtained: $\int_{\Delta S} \omega_z\, r\, \mathrm{d}r\, \mathrm{d}\chi = \Gamma$. Because the vorticity is not zero only at the axis of an infinitely thin vortex filament with coordinates $(r = a,\ \chi = \chi_0)$, the integrand is apparently expressed through the Dirac δ-functions: $\omega_z = \Gamma\, \delta(r - a)\, \delta(\chi - \chi_0)/r$. Correspondingly, (3.13) takes the form

$$\Delta^* \Psi = 2B^4 w_0/l - \omega_z = \Gamma\, \delta(r - a)\, \delta(\chi - \chi_0)/r. \tag{3.18}$$

Using the method of the separation of variables (see, Okulov 1995), the solution of (3.18) for the stream function is found in the form of infinite series

$$\Psi = \frac{w_0 r^2}{2l} - \frac{\Gamma}{4\pi} \left\{ \begin{matrix} a^2/l^2 + \ln a^2 \\ r^2/l^2 + \ln r^2 \end{matrix} \right\} - \frac{\Gamma a r}{\pi l^2} \sum_{m=1}^{\infty} m \left\{ \begin{matrix} I'_m(mr/|l|) Z'_m(ma/|l|) \\ I'_m(ma/|l|) Z'_m(mr/|l|) \end{matrix} \right\} \cos m(\chi - \chi_0), \tag{3.19}$$

where $z_m(x) = K_m(x) - a_m I_m(x)$ and $a_m(x) = K'_m(mR/|l|)/I'_m(mR/|l|)$ are selected so as to satisfy condition (3.14); $I_m(x)$ and $K_m(x)$ are the modified Bessel's functions

(the prime signifies the derivative). Here and below, the upper and lower lines in the brackets correspond to the cases $r < a$ and $r \geqslant a$ respectively.

Substituting (3.19) into (3.11), we can write the components of the velocity vector as

$$\left.\begin{aligned} w_\varphi &= \frac{\Gamma}{2\pi r}\left\{\begin{matrix}0\\1\end{matrix}\right\} + \frac{\Gamma a}{\pi r|l|}\sum_{m=1}^{\infty} m \left\{\begin{matrix} I_m(mr/|l|)Z'_m(ma/|l|) \\ I'_m(ma/|l|)Z_m(mr/|l|)\end{matrix}\right\}\cos m(\chi-\chi_0),\\ w_z &= w_0 - \frac{\Gamma}{2\pi l}\left\{\begin{matrix}0\\1\end{matrix}\right\} - \frac{\Gamma a}{\pi|l|}\sum_{m=1}^{\infty} m \left\{\begin{matrix} I_m(mr/|l|)Z'_m(ma/|l|) \\ I'_m(ma/|l|)Z_m(mr/|l|)\end{matrix}\right\}\cos m(\chi-\chi_0),\\ w_r &= -\frac{\Gamma a}{\pi l^2}\sum_{m=1}^{\infty} m \left\{\begin{matrix} I'_m(mr/|l|)Z'_m(ma/|l|) \\ I'_m(ma/|l|)Z'_m(mr/|l|)\end{matrix}\right\}\sin m(\chi-\chi_0). \end{aligned}\right\} \quad (3.20)$$

Note that when $R\to\infty$ we deal with the case of a helical filament in unbounded space. Then $a_m\to 0$ and solution (3.20) for velocity components w_r and w_φ coincides completely with the results by Hardin (1982). The value of w_z differs only by the constant w_0 that represents a translatory flow along the z-axis.

For error-free computation of the velocity field and the stream function it is appropriate to separate the singularities from the solution in explicit form:

$$\Psi = \frac{\Gamma}{4\pi}(G+H), \quad (3.21)$$

The singular term G is expressed through the elementary functions

$$G = -C_{ar}\ln\frac{\tilde{a}^2+\tilde{r}^2-2\tilde{r}\tilde{a}\cos(\chi-\chi_0)}{(\tilde{R}^4/\tilde{a}^2)+\tilde{r}^2-2\tilde{r}(\tilde{R}^2/\tilde{a})\cos(\chi-\chi_0)} \quad (3.22)$$

where $\tilde{x} = 2x\exp[C_x-1]/(C_x+1)$ may be interpreted as distorted radial distances, $C_x = (1+x^2/l^2)^{1/2}$, $C_{ar} = (C_aC_r)^{1/2}$. Here symbol x denotes a, r or R. The regular remainder in (3.21) has the form

$$H = \beta\frac{r^2}{l^2} - \left\{\begin{matrix} a^2/l^2+\ln a^2 - C_{ar}\ln\tilde{a}^2 \\ r^2/l^2+\ln r^2 - C_{ar}\ln\tilde{r}^2\end{matrix}\right\} - \frac{4ra}{l^2}\sum_{m=1}^{\infty}\left\{\begin{matrix} B_m(r,a)\\ B_m(a,r)\end{matrix}\right\}\cos m(\chi-\chi_0), \quad (3.23)$$

where

$$B_m(x,\,y) = I'_m\left(\frac{mx}{|l|}\right)Z'_m\left(\frac{my}{|l|}\right) - \frac{C_{a,r}}{2mra}\left[\left(\frac{\tilde{x}}{\tilde{y}}\right)^m - \left(\frac{\tilde{x}\tilde{y}}{\tilde{R}^2}\right)^m\right], \quad \beta = 2\pi l w_0/\Gamma.$$

The singular summand G contains the general information on the character of the flow depending on the vortex parameters and permits a qualitative flow analysis. Nonetheless, the existence of a singularity in the basic representation of the stream function through series (3.19) does not allow the use of the differentiation operation on formula (3.22) to obtain the expressions for the velocity components. Because of this the main singularity of a velocity field (pole-like) is separated immediately in series (3.20) for velocity components:

$$\left.\begin{aligned} w_r &= \frac{\Gamma a}{\pi l^2}(S_r+R_r),\\ w_\varphi &= \frac{\Gamma}{2\pi r}\left\{\begin{matrix}0\\1\end{matrix}\right\} + \frac{\Gamma a}{\pi r|l|}\left(S_\chi+R_\chi\right),\\ w_z &= w_0 - \frac{\Gamma a}{2\pi l}\left\{\begin{matrix}0\\1\end{matrix}\right\} - \frac{\Gamma a}{\pi l|l|}\left(S_\chi+R_\chi\right). \end{aligned}\right\} \quad (3.24)$$

S_r and S_χ are also written through the elementary functions of distorted radial distances:

$$\left.\begin{aligned} S_r = & -\frac{C_{ar}l^2}{2ra}\left(\frac{\tilde{r}\tilde{a}\sin(\chi-\chi_0)}{\tilde{r}^2+\tilde{a}^2-2\tilde{r}\tilde{a}\cos(\chi-\chi_0)}\right. \\ & \left.-\frac{\tilde{r}(\tilde{R}^2/\tilde{a})\sin(\chi-\chi_0)}{(\tilde{R}^4/\tilde{a}^2)+\tilde{r}^2-2\tilde{r}(\tilde{R}^2/\tilde{a})\cos(\chi-\chi_0)}\right), \\ S_\chi = & \frac{C_{a/r}|l|}{2ra}\left(\begin{Bmatrix} 0 \\ -1 \end{Bmatrix}+\frac{\tilde{r}^2-\tilde{r}\tilde{a}\cos(\chi-\chi_0)}{\tilde{r}^2+\tilde{a}^2-2\tilde{r}\tilde{a}\cos(\chi-\chi_0)}\right. \\ & \left.-\frac{\tilde{r}^2-\tilde{r}(\tilde{R}^2/\tilde{a})\cos(\chi-\chi_0)}{(\tilde{R}^4/\tilde{a}^2)+\tilde{r}^2-2\tilde{r}(\tilde{R}^2/\tilde{a})\cos(\chi-\chi_0)}\right) \end{aligned}\right\} \tag{3.25}$$

where $C_{a/r} = \left(C_a/C_r\right)^{1/2}$, and remainders of series take the form

$$R_r = \sum_{m=1}^{\infty} m \begin{Bmatrix} B_m(r,a) \\ B_m(a,r) \end{Bmatrix} \sin m(\chi-\chi_0), \quad R_\chi = \sum_{m=1}^{\infty} \begin{Bmatrix} B_m^I \\ B_m^Z \end{Bmatrix} \cos m(\chi-\chi_0) \tag{3.26}$$

Here

$$B_m^I = I_m\left(\frac{mr}{|l|}\right) Z_m'\left(\frac{ma}{|l|}\right) + \frac{C_{a/r}\,|l|}{2ma}\left[\left(\frac{\tilde{r}}{\tilde{a}}\right)^m - \left(\frac{\tilde{r}\tilde{a}}{\tilde{R}^2}\right)^m\right],$$

$$B_m^Z = I_m'\left(\frac{ma}{|l|}\right) Z_m\left(\frac{mr}{|l|}\right) + \frac{C_{a/r}\,|l|}{2ma}\left[-\left(\frac{\tilde{a}}{\tilde{r}}\right)^m - \left(\frac{\tilde{r}\tilde{a}}{\tilde{R}^2}\right)^m\right].$$

An analysis of (3.22)–(3.26) shows that when $|l| \to \infty$ the solutions obtained coincide with the solution for a rectilinear vortex in a cylinder or a point vortex in a circle (Lamb 1932).

It was established numerically that for a wide range of geometrical parameters of a vortex filament, the remainders of series (3.23) and (3.26) are relatively small in comparison to the main singular parts (3.22) and (3.25) in representations of the stream function (3.21) and the velocity field (3.24). Hence the first of them may be neglected. Owing to the simplicity of expressions (3.22) and (3.25) it was possible to illustrate the flow considered for a wide range of vortex filament parameters. The flow analysis was carried out on the basis of constructing both the iso-lines of a stream function and projections of stream surfaces (stream tubes) on cross-sectional and axial-sectional planes.

In figure 5 a comparison is made for iso-lines $\Psi = \text{const}$ in an unbounded space (a) and in a tube (b) for helix radius $a = 0.9$, velocity at flow axis $w_0 = \Gamma/h$, circulation $\Gamma = 1$, and helix pitch $h = 2$. All quantities are made dimensionless by tube radius R and flow rate Q. As is seen the influence of the wall on the flow pattern is fairly significant.

Figure 6 demonstrates the effect of h and w_0 on the projections of streamlines on horizontal and vertical sections of a tube (the projections of velocity vectors on corresponding planes are directed along the tangent to these curves). Note that w_0 does not influence the pattern of streamlines in the cross-section of the tube. As follows from formula (3.20) for w_z, the contribution of w_0 may be interpreted as the transition to a coordinate system moving with speed $(-w_0)$ along the z-axis. So the pattern of streamlines in the longitudinal section of the tube is defined fully by w_0 for other parameters fixed. It is clear that w_0 is related to the flow rate through the tube and therefore it is of fundamental importance for interpretation of the swirl flow regimes in a bounded space. For example, for $w_0 = 0$, $h = 1$ the axial motion near the tube

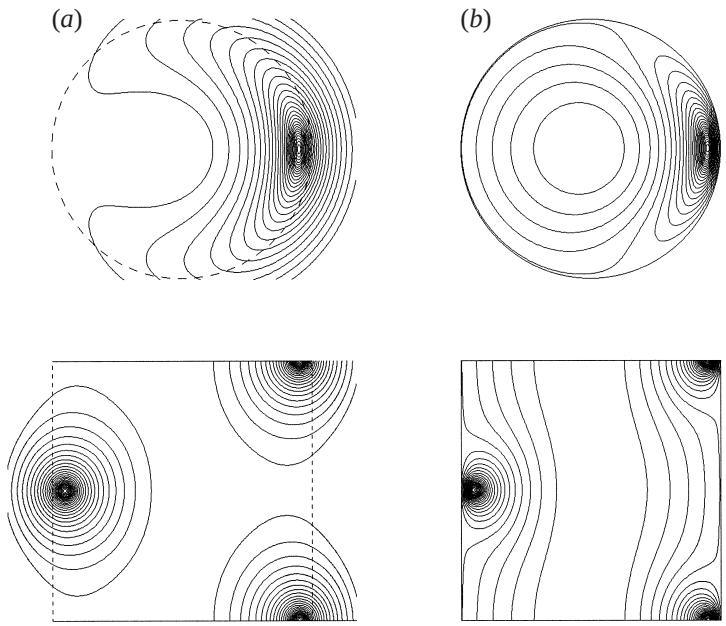

FIGURE 5. Iso-lines Ψ = const (in the horizontal and vertical planes) for an infinitely thin helical vortex filament in an unbounded space (*a*) and in a tube (*b*); - - -, imaginary boundaries of the tube in the space. The filament parameters: $a = 0.9$, $w_0 = \Gamma/h$, $\Gamma = 1$, $h = 2$. All the quantities are made dimensionless by tube radius R and flow rate Q (this is also true for figures 8, 9, 11, 12).

axis is absent but there is intense axially directed flow in the vicinity of the tube wall. At $w_0 = \Gamma/h$, $h = 1$, on the other hand, the axial flow is absent near the wall and exists inside the helix. Finally, at $w_0 = 0.5 = \Gamma/h$, $h = 1$ the liquid outside and inside the helix moves along the z-axis in opposite directions.

The effect of helix radius a on the streamline pattern in a tube is shown in figure 7 for different w_0. If helix radius and velocity at the tube axis are small ($a = 0.1$, $w_0 = 0$) the flow pattern is close to the case of a rectilinear vortex filament. However, by increasing w_0 even at small a the effect of curving the filament is seen even in the vicinity of the wall (see, $w_0 = \Gamma/h$, $a = 0.1$). With the increase of the helix radius the streamlines in the cross-section differ more strongly from the circular form, and the flow pattern in the longitudinal plane (as in figure 6) is defined fully by the value of w_0.

Examples of calculating multi-vortex structures are described in § 6.2.

4. Axisymmetrical (columnar) helical vortices

4.1. *One-dimensional flow with helical symmetry*

We start considering this class of helical vortices with a finite size core with the simplest particular case of axisymmetrical or columnar vortices. Our approach may be clearly demonstrated by the example of comparison of the helical columnar vortex with the Rankine vortex (figure 8): namely the Rankine vortex consists of uniformly distributed rectilinear vortex filaments (figure 8*a*); the axisymmetrical helical vortex in our model is a superposition of *the helical vortex filaments* (figure 8*b*,*c*).

If the vorticity distribution over the vortex filaments is given, the problem of finding the velocity field is reduced to integrating the expressions (3.20). On the other

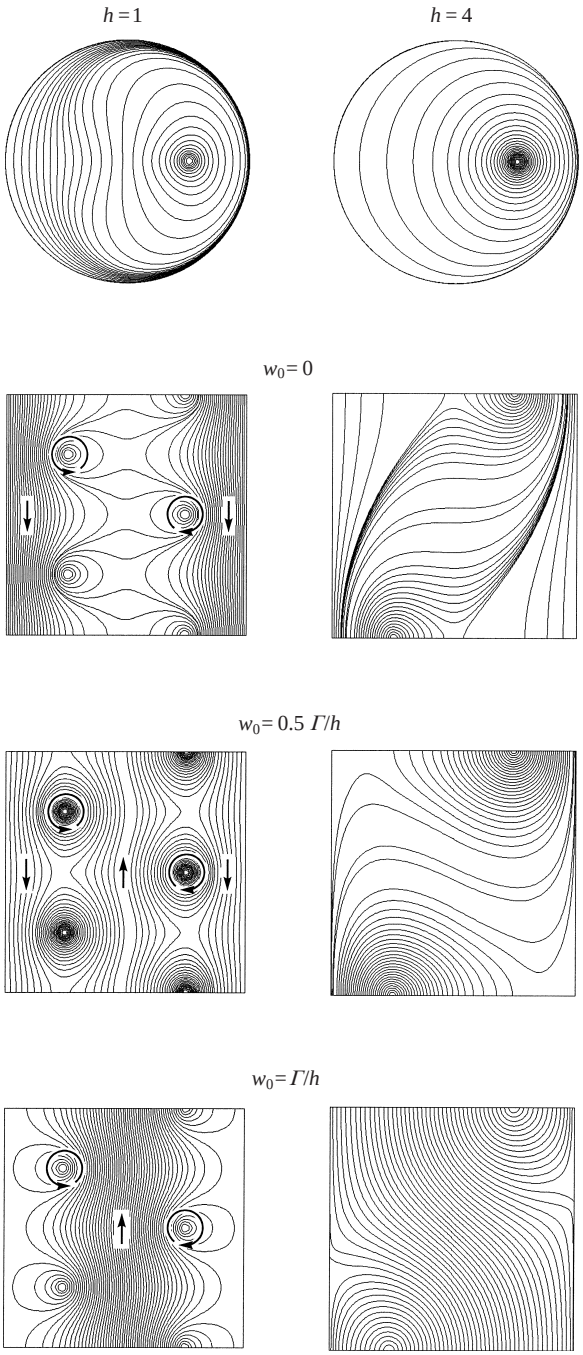

FIGURE 6. The effect of h and w_0 on the streamlines (projections) for the case of a helical vortex filament in a tube at $a = 0.5$. Arrows show the direction of the flow.

hand, this task may be solved without invoking the results of § 3.3. An analysis of the governing equations shows that the condition of axial symmetry allows the development of a fairly general model of axisymmetrical helical vortices in a rigorous treatment. We assume $\partial/\partial\chi \equiv 0$, $w_r \equiv 0$. Therefore the Helmholtz equation (3.12)

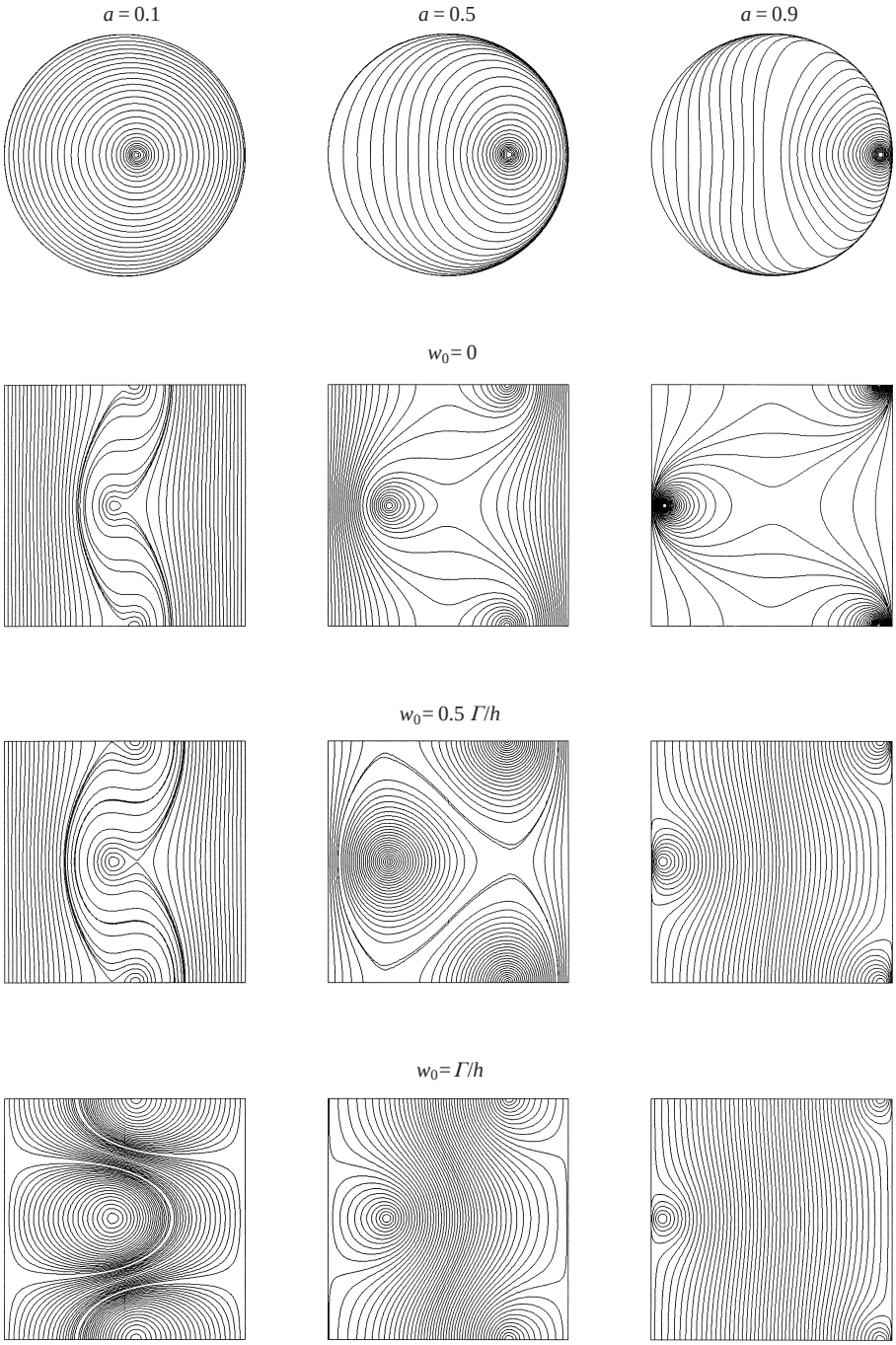

FIGURE 7. The effect of a and w_0 on the streamlines (projections) for the case of a helical vortex filament in a tube at $h = 2$.

satisfies any radial distribution of the axial component of the vorticity. It follows from the vorticity definition that

$$w_\varphi = \frac{1}{r}\int_0^r \omega_z(r)\, r\, \mathrm{d}r. \tag{4.1}$$

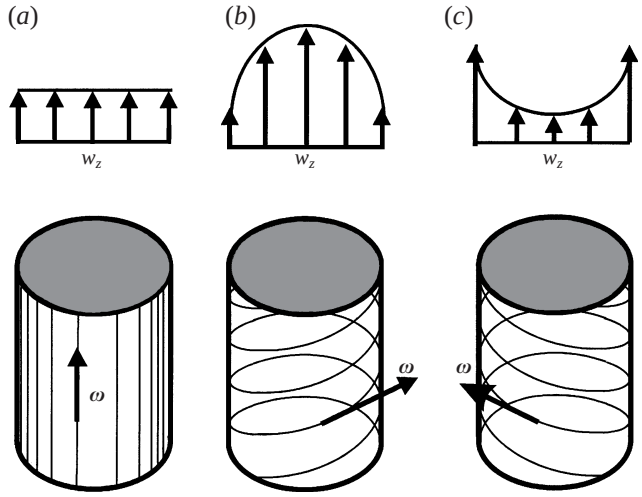

FIGURE 8. Models of columnar vortices with uniform distribution of the elementary vortex filaments within the core. (*a*) Rankine vortex consisting of rectilinear filaments. (*b*) A columnar vortex consisting of right-handed helical vortex lines. (*c*) A columnar vortex consisting of left-handed helical vortex lines.

Since the axial component of the velocity remains connected with w_φ by relation (3.9), the expression for w_z may be written as

$$w_z = w_0 - \frac{1}{l}\int_0^r \omega_z(r)\, r\, \mathrm{d}r. \tag{4.2}$$

The condition of axial symmetry significantly simplifies the problem of determining the static pressure from the Euler equations. Actually, (3.4) becomes an identity and (3.3) is reduced to the equation $\rho w_\varphi^2 / r = \partial p/\partial r$, from which

$$p = p_0 + \rho \int_0^r w_\varphi^2 \frac{\mathrm{d}r}{r}. \tag{4.3}$$

Here p_0 is the static pressure at the tube axis. It is seen from (4.3) that the axial component of the velocity does not influence the pressure in swirling axisymmetric flow. Furthermore, this important feature will be used for the estimation of vortex parameters from the distribution of the bottom pressure (see § 4.2).

We shall consider three important examples of the simplest distributions of vorticity: uniform, hat-type and Gaussian (see table 1). From (4.1) and (4.2) the velocity components may be written as

$$w_\varphi = \frac{\Gamma}{2\pi r}\Phi(r), \quad w_z = w_0 - \frac{\Gamma}{2\pi l}\Phi(r), \quad \Phi(r) = \frac{2\pi}{\Gamma}\int_0^r \omega_z(r)\, r\, \mathrm{d}r. \tag{4.4}$$

As seen from table 1 and (4.4) profiles of the circumferential velocity as well as the pressure distribution coincide with the corresponding ones in Rankine, Scully and Lamb vortices (Hopfinger & van Heijst 1993, Scully 1975). At the same time the axial velocity non-uniformly varies with the radius and is inversely proportional to the pitch of helical symmetry.

For the step-like distribution function we can consider a more general case with

Model	I	II	III
$\omega_z \dfrac{\pi\varepsilon^2}{\Gamma}$	$\begin{cases} 1, & r < \varepsilon \\ 0, & r \geqslant \varepsilon \end{cases}$	$\left(1+\dfrac{r^2}{\varepsilon^2}\right)^{-2}$	$\exp\left(-\dfrac{r^2}{\varepsilon^2}\right)$
$\Phi(r)$	$\begin{cases} r^2/\varepsilon^2, & r < \varepsilon \\ 1, & r \geqslant \varepsilon \end{cases}$	$\dfrac{r^2}{r^2+\varepsilon^2}$	$1-\exp\left(-\dfrac{r^2}{\varepsilon^2}\right)$
$\dfrac{\Delta p}{\rho}\dfrac{8\pi^2\varepsilon^2}{\Gamma}$	$\begin{cases} r^2/\varepsilon^2, & r < \varepsilon \\ 2-\varepsilon^2/r^2, & r \geqslant \varepsilon \end{cases}$	$\dfrac{r^2}{r^2+\varepsilon^2}$	$2\ln 2-\dfrac{\varepsilon^2}{r^2}\left(1-\exp\left(-\dfrac{r^2}{\varepsilon^2}\right)\right)^2$ $+2\mathrm{Ei}\left(-\dfrac{r^2}{\varepsilon^2}\right)-2\mathrm{Ei}\left(-2\dfrac{r^2}{\varepsilon^2}\right)$

TABLE 1. Dimensionless vorticity, velocity function and pressure for the three models of a columnar vortex.

the vorticity distributed over the annular section $b_1 \leqslant r \leqslant b_2$:

$$\omega_z = \frac{\Gamma}{\pi(b_2^2-b_1^2)}\begin{cases} 0, & r < b_1,\ r > b_2 \\ 1, & b_1 \leqslant r \leqslant b_2 \end{cases} \quad \text{with} \quad \Phi(r) = \begin{cases} 0, & r < b \\ \dfrac{r^2-b_1^2}{b_2^2-b_1^2}, & b_1 \leqslant r \leqslant b_2 \\ 1, & r > b_2. \end{cases}$$

Such 'hollow' vortices may appear under the near-wall flow swirling and will be used below for constructing more complex models of vortices (see § 4.2). The pressure field for the annular helical vortex takes the form

$$p = p_0 - \frac{\rho\Gamma^2}{8\pi^2}\begin{cases} 0, & r < b_1 \\ \dfrac{1}{\left(b_2^2-b_1^2\right)^2}\left(\dfrac{r^4-b_1^4}{r^2}-4b_1^2\ln\dfrac{r}{b_1}\right), & b_1 \leqslant r \leqslant b_2 \\ -\dfrac{1}{r^2}+\dfrac{2}{b_2^2-b_1^2}-\dfrac{4b_1^2}{\left(b_2^2-b_1^2\right)^2}\ln\dfrac{b_2}{b_1}, & r > b_2, \end{cases}$$

Unlike the Rankine vortex, this model allows for a great variety of axial velocity distributions depending on the value and sign of vortex pitch l and the velocity at the axis w_0. In the limit case of $l \to 0$, $\Gamma \to 0$, $\Gamma/l = \text{const}$, $(b_2 - b_2) \to 0$ the annular vortex degenerates into a vortex sheet localized at the cylindrical surface $r = b_2 = b_2$ inducing axial velocity only.

The velocity field for the Gaussian vorticity distribution

$$w_\varphi = \frac{\Gamma}{2\pi r}\left[1-\exp\left(-r^2/\varepsilon^2\right)\right], \quad w_z = w_0 - \frac{\Gamma}{2\pi l}\left[1-\exp\left(-r^2/\varepsilon^2\right)\right] \tag{4.5}$$

is shown to have the same structure as the empirical relations which have been widely used for processing experimental data on swirl flow (Faler & Leibovich 1977; Leibovich 1978, 1984; Escudier 1988; Alekseenko & Shtork 1992):

$$w_\varphi = \frac{K}{r}\left(1-\exp\left(-\alpha r^2\right)\right), \quad w_z = W_1 + W_2\exp\left(-\alpha r^2\right) \tag{4.6}$$

where K, W_1, W_2, α are empirical constants. The swirl velocity distribution in (4.6) corresponds exactly to the vortex found by Burgers (1940) which is the solution of

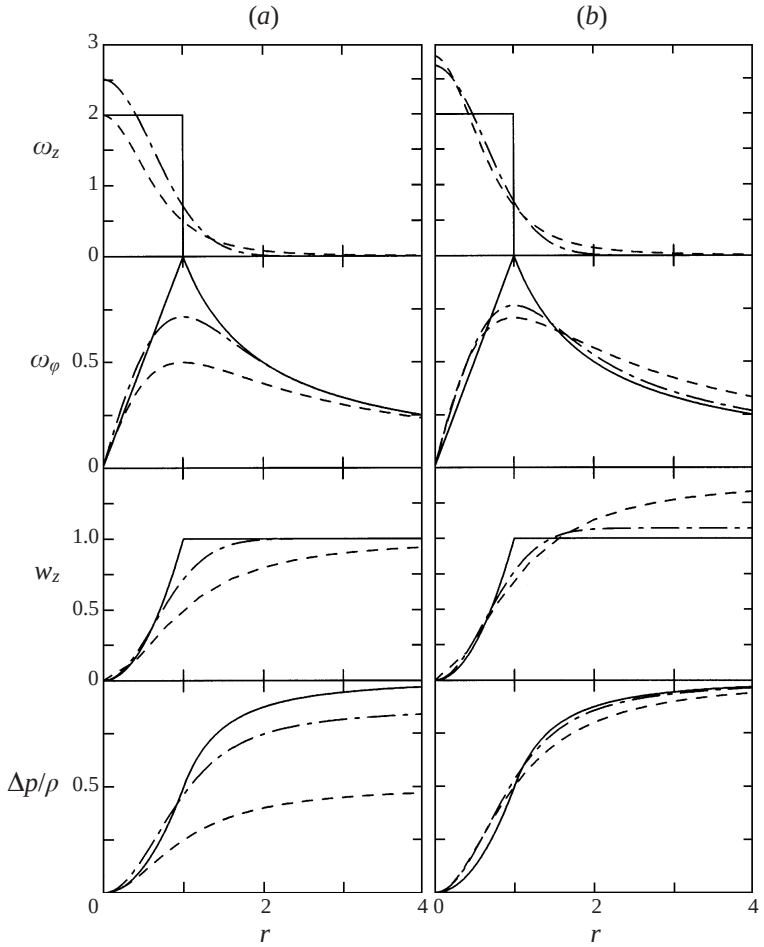

FIGURE 9. The radial profiles of tangential, w_φ, and axial, w_z, velocity components and pressure drop, $\Delta p/\rho$, in the columnar vortices with various distributions of the axial component of vorticity, ω_z: ——, ω_z is constant in the core; -·-·-, hat-type dependence; - - -, Gaussian distribution. Comparison of the models is made for conditions: (*a*) circulation, Γ, is the same, (*b*) the pressure difference between the vortex centre and periphery is the same.

the Navier–Stokes equations. The axial component is similar to that found in a far wake (see, Lessen, Singh & Paillet 1974).

Profiles (4.6) have not been considered previously as the unified solution of fluid motion equations. A direct comparison of the exact solution (4.5) and empirical formulae (4.6) yields

$$\Gamma = 2\pi K; \quad l = K/W_2; \quad w_0 = W_1 + W_2; \quad \varepsilon = \alpha^{-1/2}.$$

Thus, the theoretical solution obtained makes the refinement of the physical sense of the empirical constants possible and explains the good agreement between formulae (4.6) and the experiment. When comparing (4.5) with the experiment, it is better to use the radius of the location of swirl velocity maximum $r_m = \varepsilon\sqrt{1.256}$ instead of scale ε.

In figure 9 all three solutions presented in table 1 are compared in two different ways. It is assumed that $w_0 = 0$ and $l = -1$. The value of ε is chosen from the

requirement of the same values of r_m ($\varepsilon = 1$ for columns I, II in table 1 and $\varepsilon = 1/1.12$ for column III). The first method of comparison is to compare vortices with the same circulation $\Gamma = 2\pi$. As follows from figure 9(a), solutions I and III are the closest to each other. Solution I has a more simple and vivid form since one can easily determine the core size from the break point of the velocity profile. Because of this we prefer to use model I for further analysis. The essential difference of the models I and III from II is explained by the fact that the vorticity in the last vortex is less concentrated.

A more correct comparison from our point of view may be made if the same values of the pressure difference Δp at the vortex axis and periphery ($r \to \infty$) are used for the vortices compared. But then the vortex circulations will be different:

$$\Gamma_1 = 2\pi, \quad \Gamma_2 = 2\pi\sqrt{2}, \quad \Gamma_3 = 2\pi/(1.256 \ln 2)^{1/2}.$$

In such a case the profiles of vorticity, velocity and pressure in all three solutions start to correspond to each other better (especially for pressure, see figure 9b). An important fact follows from comparing the calculated pressure distributions at the point of the swirl velocity maximum r_m. For vortices I and II the point r_m coincides with the point $r_{0.5}$ where the pressure equals half of the difference between the values of pressure at the vortex axis and the periphery. Analysing the pressure distribution for vortex III one can see that here points r_m and $r_{0.5}$ also almost coincide. Consequently the vortex radius may be determined as the point where pressure equals half of the full pressure drop. Recall that the pressure in the experiment is reckoned from its value at the bottom.

Thus generalized models of columnar helical vortices can be developed from the arbitrary distribution of an axial vorticity component along the radial coordinate. They generalize the known models by Rankine, Lamb, Burgers etc. and permit one to obtain various profiles for both tangential and axial components of velocity.

4.2. *Experimental study of vortices with a rectilinear axis*

The main purpose of the work is to study helical vortices, primarily vortex filaments of helical form. Hence the initial experimental task was to generate swirl flows with a vortex filament (or, otherwise, concentrated vortices). In any vortex chamber, concentrated vortices are formed by putting a diaphragm in the exit orifice (Escudier, Bornstein & Zehnder 1980; Shtym 1985). Here we shall consider in detail the formation of the vortex filament in the tangential chamber, shown in figure 1, with an exit orifice diameter of 40 and 70 mm.

The most remarkable feature of the swirl flow in a chamber with a diaphragmed exit is the localization of vorticity near the chamber axis. The smaller the diameter of the exit orifice, the greater the effect. A sharp increase in the axial component of vorticity $\omega_z = \Gamma/\pi\varepsilon^2$ at the chamber centre occurs due to the decreasing ε and is accompanied by a drastic pressure drop at the axis (see table 1). Owing to the last effect a cavity appears at the vortex axis in the form of a continuous thin air filament of constant thickness with diameter up to 0.1 mm (figure 10). The air filament is formed of tiny air bubbles introduced into the liquid with the purpose of flow visualization; and this filament extends from the bottom to the exit orifice (and further). By decreasing the air supply and for a low flow rate of liquid the air filament becomes so thin that it breaks into separate tiny bubbles which may be used as particle markers for flow visualization. By this means the formation of a gaseous cavity is an effective way of visualizing the axes of concentrated vortices in fluid.

The experimental data on the profiles of tangential and axial velocities are presented in figure 11 for $d_e = 40$ mm. In this case the vortex radius is 1.8 mm and measurements

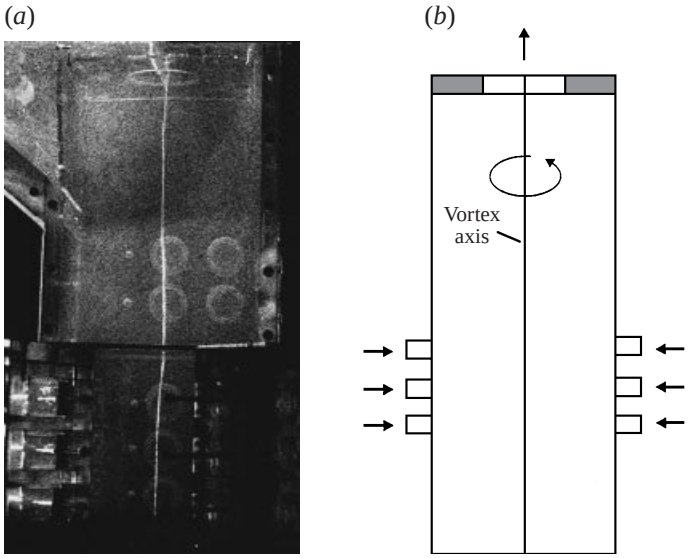

FIGURE 10. Visualization (*a*) and schematic (*b*) of a flow with the generation of a concentrated vortex with a rectilinear axis. $d_e = 70$ mm, $z_e = 560$ mm, $Re = 10^4$, $S = 2.9$. The light line in the photograph is the air filament visualizing the vortex axis.

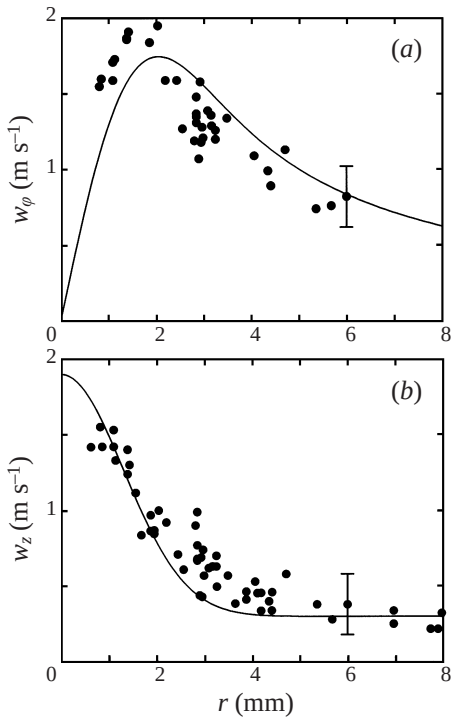

FIGURE 11. Profiles of the tangential (*a*) and axial (*b*) velocity components in a vortex chamber with a small exit orifice. $d_e = 40$ mm, $z_e = 430$ mm, $Re = 8 \times 10^3$, $S = 3$. ●, experimental points; ——, empirical formula (4.6).

may be taken only with the method of stroboscopic visualization. The velocity distributions can be described using empirical dependencies (4.6) with the following constants: $K = 5$, $W_1 = 0.3$, $W_2 = 1.6$ and $\alpha = 0.3$. The experimental profiles permit the classification of the observed rectilinear vortex as a vortex filament since the vortex diameter (3–10 mm) is much less than the vortex length (430–560 mm) and the cross-sectional size of the chamber (188 mm).

To apply the exact solutions presented in table 1 to the description of experimental profiles, it is necessary to know the basic characteristics of the vortex: circulation Γ, core size ε, pitch of helical symmetry l, and velocity at the vortex axis w_0. Of course, they may be recalculated through the empirical constants K, W_1, W_2 and $\alpha = 0.3$; however it should be noted that some approximations are required to determine the constants. So, Garg & Leibovich (1979) generalize the experimental data with relation (4.6) using the method of least squares. Because of this, preference must be given to direct methods of determining the vortex model parameters. The methods of calculating l and w_0 have been described in § 3.2 and the procedure for finding Γ and ε will be given below.

In vortex models I and II assumed in § 4.1, ε coincides with r_m and for model III $\varepsilon = r_m/1.12$, i.e. ε may be considered known if r_m is measured in the experiment. Also if we know the value of maximum velocity $w_{\varphi\max}$ the circulation is determined using the formulae

$$\Gamma = 2\pi r_m w_{\varphi\max} \text{ for I and II;} \quad \Gamma = 4\pi r_m w_{\varphi\max}/0.715 \text{ for III.}$$

By this means the vortex models will be completely defined if in addition to l and w_0 the location and value of maximum tangential velocity is known.

One can calculate ε and Γ through the pressure distributions. If we find point $r_{0.5}$ then according to the theoretical models of the previous section it may be identified with the point r_m. On the other hand if the value of the pressure drop Δp_0 is known the circulation may be determined as $\Gamma = \eta 2\pi r_{0.5}(\Delta p_0/\rho)^{0.5}$ with $\eta^2 = 1$, 2 and $1/\ln 2$ for these three models respectively.

In general it is very difficult to determine the characteristics of both the velocity field and the static pressure field due to the small size of the core, the three-dimensionality of the flow with helical vortices and the ever present unsteadiness (in particular, precessing motion and turbulence). Nonetheless, some vortex parameters may be estimated with relative ease by measurement, for example, of the bottom pressure (Kutateladze *et al.* 1987). It should be expected, due to thin boundary layer, that the distributions of static pressure at the chamber bottom and the flow core (in the vicinity of the bottom) would be identical. Of course, the case of vortex breakdown, which appears in flows with a marked value of the axial pressure gradient (Escudier 1988), should be excluded. In the absence of vortex breakdown one can reconstruct the swirl velocity field and determine the other characteristics, in particular the vortex core size, using pressure measurements.

In figure 12 the radial distributions of static pressure at different cross-sections of the chamber and at the bottom are compared. It is clear that the head tube is not acceptable for measuring in the vicinity of the vortex axis. Nonetheless comparison of experimental data in areas available for measurements shows that the pressure profiles do not change with chamber height and correspond to the bottom pressure. A similar conclusion was reached by Kutateladze *et al.* (1987) for a diaphragmed chamber of different construction. Because of this we shall analyse the data on the bottom pressure and try to use them for the estimation of the parameters of a vortex filament interacting with a flat bottom.

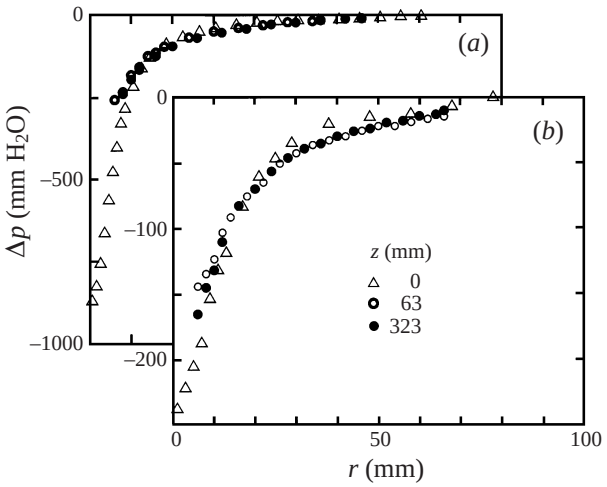

FIGURE 12. Pressure distributions at different cross-sections of the chamber for diameter of the exit orifice $d_e = 70$ mm (a) and 100 mm (b). $z_e = 430$ mm, $Re = 2.8 \times 10^3$, $S = 3$. The points for $z = 0$ correspond to the bottom pressure.

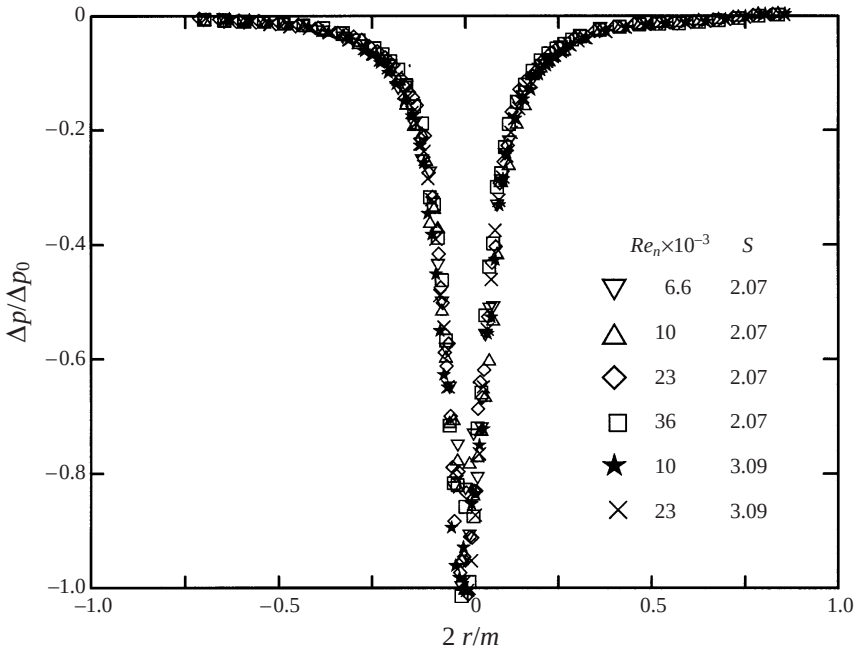

FIGURE 13. Generalized profiles of the bottom pressure for different values of the Reynolds number and swirl parameter. $d_e = 70$ mm, $\Delta p_0 = |p_0 - p_\infty|$, where p_0 and p_∞ are the values of the static pressure at the vortex axis and periphery.

In figure 13 the data on bottom pressure are generalized in the coordinates [$\Delta p/\Delta p_0$, $2r/m$] for different values of Reynolds number Re_n and swirl parameter S. The diameter of the exit orifice d_e was fixed and equal to 70 mm. Here $\Delta p_0 = |p_0 - p_\infty|$, p_0 is the pressure at the vortex axis, p_∞ is the pressure at the periphery (at the sidewall of a channel), Reynolds number $Re_n = V_n d_n/\nu$, V_n is the velocity at the nozzle exit, d_n is the hydraulic diameter of the nozzle.

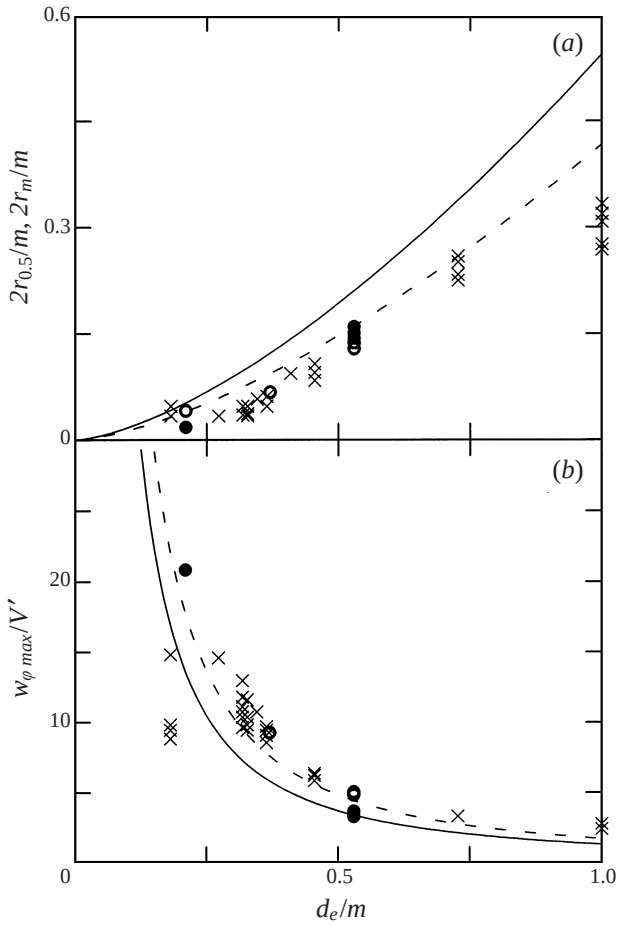

FIGURE 14. Characteristic scales of the transversal size (a) and velocity (b) for the concentrated vortex. r_m is the coordinate of maximum tangential velocity $w_{\varphi\,\max}$, $r_{0.5}$ is the coordinate of the point where pressure equals half of the full pressure drop. ×, Data by Escudier *et al.* (1980) ($S = 1.8$); ●, measured values ($S = 3.1$); ○, measurements (a) or calculations (b) by the measured pressure profiles with the Rankine model. (a), ○, $2r_{0.5}/m$, other symbols and lines correspond to $2r_m/m$; calculations according to (4.7): ——, $S = 3.1$, - - -, $S = 1.8$. (b) Symbols show experimental data; calculations according to (4.8): ——, $S = 3.1$, - - -, $S = 1.8$.

In figure 14(a) the experimental data on r_m and $r_{0.5}$ are shown against the diameter of the exit orifice d_e. The scale r_m is usually identified with the radius of the concentrated vortex. Here our data coincide with measurements by Escudier *et al.* (1980) for a vortex tube with a slot entrance. The coincidence of the values of r_m and $r_{0.5}$ is the most remarkable fact. This means that the vortex radius may be determined from the point where the static pressure equals half of the full pressure drop. The same conclusion follows from the above analysis of theoretical models.

Attempts to theoretically calculate r_m have been made by Abramovich (1951) on the basis of the maximum flow rate principle and by Goldshtick (1981) by using the principle of minimum flux of kinetic energy. Formulae are obtained in which the relative size of a vortex $2r_m/d_e$ is expressed through the construction parameter of a vortex chamber $m_c = 4\Sigma'/(\pi d_e d)$, where Σ' is the area of the nozzle cross-section, d is the diameter of the conventional circumference (see figure 1). It is more convenient

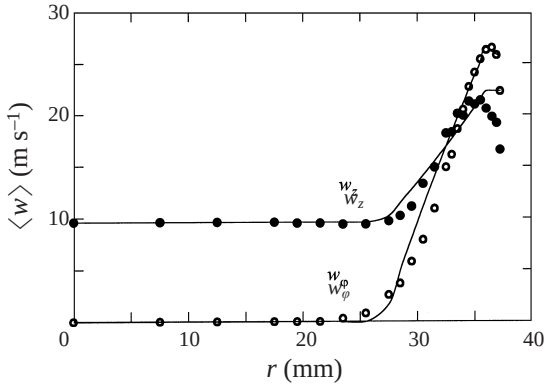

FIGURE 15. Comparison of experimental data by Kutateladze *et al.* (1987) (near-wall swirl jet in a channel with an open endwall, $x = 46$ mm) with a vortex model with an annular distribution of vorticity. ○, ●, experiment; ——, formula (4.4).

to use the simple empirical formula by Ovchinnikov & Nikolaev (1973):

$$2r_m/d_e = 0.35m_c^{-1/2} \tag{4.7}$$

which is valid for $d_e/2R_c > 0.1$ and $m_c > 0.1$. Here R_c is the vortex chamber radius.

The measured values of the maximum tangential velocity are presented in figure 14(b), also in the form of dependence on the diameter of the exit orifice. V' is the velocity component at the nozzle exit parallel to the tangential velocity in the chamber.

A simple evaluation of $w_{\varphi\max}$ may be made on the basis of profile (4.5) assuming that it is valid up to the wall, i.e. $r = R_c$ (Goldshtick 1981). As this is the case, V' is considered to be the velocity at the wall

$$w_{\varphi\max}/V' = 0.715R_c/r_m. \tag{4.8}$$

r_m may be calculated, for example, by using empirical formula (4.7) or in other ways. So the calculated curves in figure 14(b) are obtained with (4.8) by using the model by Goldshtick (1981) for r_m. Otherwise, the maximum tangential velocity may be determined by rarefaction Δp_0 at the vortex centre, for example, with the Rankine model: $w_{\varphi\max} = (\Delta p_0/\rho)^{1/2}$. The values of $w_{\varphi\max}$ calculated by these means are in good agreement with the direct measurements (see open circles in figure 14b). The level of rarefaction depends strongly on the swirl parameter, the flow rate, and the diameter of the exit orifice.

The main conclusion from this analysis is that characteristics used in the theoretical model of § 4.1 can be found by means of performing the more simple experimental task of studying the interaction between a vortex and a flat bottom. Moreover it is even possible to develop heuristic models like (4.7) and (4.8) for determining vortex parameters. As for testing theoretical models, it should be noted that extensive comparisons of profile (4.6), which is equivalent to model (4.5), were made with measurements by Leibovich (1984), Escudier (1988). Since models I and III are close to each other, it should be expected that a vortex model with uniform vorticity distribution in the core would be acceptable. As an example, a comparison of an annular vortex model with the data obtained by Kutateladze *et al.* (1987) is made in figure 15. These results point to the possibility of a vortex with annular distribution of vorticity existing.

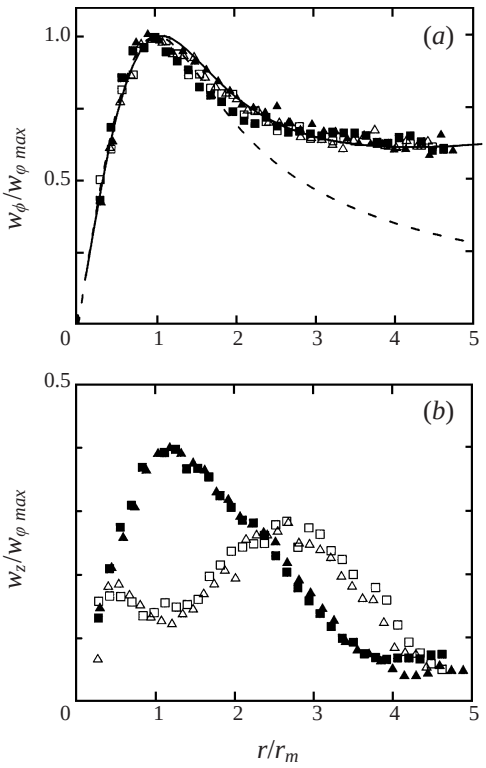

FIGURE 16. Dimensionless profiles of tangential (a) and axial (b) velocity components of flow in the vortex chamber at $d_e = 100$ mm, $S = 3.\,\triangle$, $z = 63$ mm, $Re = 2.8 \times 10^4$; ▲, 323, 2.8×10^4; □, 63, 3.5×10^4; ■, 323, 3.5×10^4; ——, empirical formula by Escudier *et al.* (1982); - - -, formula (4.6).

By this means a generalized model of an axisymmetric helical vortex with an arbitrary distribution of the axial component of vorticity along the radial coordinate (in particular, the three different cases considered) allows the obtaining of various velocity and pressure fields describing the experimental data well. Also, methods of determining the vortex parameters for these models are proposed by using measurements at the chamber bottom (or chamber endwall) where the vortex interacts with the plane.

4.3. *Vortex composition*

A qualitatively new vortex structure appears in the chamber when the orifice of the diaphragm is increased. The swirl velocity profile begins to differ fundamentally from the empirical profiles (4.6) (or the exact solution (4.5)) and a trough in the axial velocity profiles arises.

In figure 16 the velocity distributions are shown for two sections for a relatively large diameter exit orifice $d_e = 100$ mm. These data are obtained by the Pitot tube since the vortex radius is fairly large ($r_m = 14$ mm). Here r_m is determined from the location of the maximum tangential velocity $w_{\varphi\,\max}$. These results for velocity profiles as a whole correspond to measurements obtained by Escudier *et al.* (1980) with LDA in a vortex chamber with a tangential supply along the whole chamber length and also to data by Brücker & Althaus (1992) obtained with PIV in a chamber with an axial swirler. A feature of these flows is that the axial velocity has a local maximum at some

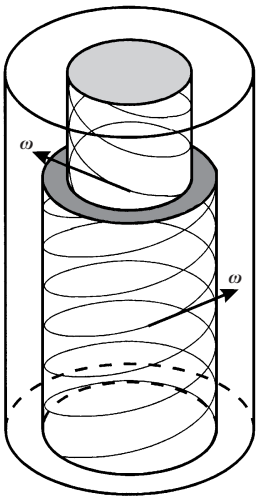

FIGURE 17. Combination of two columnar vortices.

distance from the flow axis and the tangential component deviates fundamentally from a dependence of (4.6) type. With a larger $r/r_m > 2$ the experimental points differ so strongly from (4.6) that Escudier *et al.* (1982) modified the velocity profile by the linear addition with the empirical coefficient ω_1

$$w_\varphi = \frac{K}{r}\left[1 - \exp\left(-\alpha r^2\right)\right] + \omega_1 r.$$

However the above formula does not correspond to the Burgers solution which has a clear physical sense. Attempts to describe the axial velocity profiles in a simple way failed due to their non-monotonic behaviour. Nevertheless we could solve such a problem in the framework of vortex models I and III.

Initially the question arises about the existence of helical symmetry in such complex flows. One could consider this question using the velocity profiles (figure 16) measured far away from the chamber bottom at a distance of 323 mm where the influence of the bottom is negligible. Let us divide the flow into two zones. The first zone includes the area from the axis to the point of maximum axial velocity r_*. The second zone represents the annular area between r_* and the periphery (chamber wall). With the results of § 3.2 the parameters of helical symmetry may be determined separately for each zone as follows: $l = -46.7$ mm, $w_0 = 0.12$ m s^{-1} for zone 1 and $l = 46.7$ mm, $w_0 = 0.80$ m s^{-1} for zone 2. As is seen, the pitch of helical symmetry is the same in magnitude but has a different sign (i.e. the circumferential component of the vorticity has alternating sign). This result leads to the conclusion that the fairly complex behaviour of velocity distributions may be modelled by the combination of several simple vortices. Such a composite vortex is assumed to contain two non-intersecting areas (in this case, zones 1 and 2). An example of the combination of two vortices with rectilinear axes is shown in figure 17. Here the first vortex is associated with the cylindrical area of radius $b_1 = r_*$ inside which the vorticity is constant and $\boldsymbol{\omega}$ is directed at some angle to the z-axis (left vortex). The second vortex is localized in an annular area with the radii b_1 and b_2 inside which the vorticity is also constant but the vorticity vector is oppositely oriented (right vortex). The resulting velocity field is determined as the sum of the contributions from the two vorticity areas due to the linear relation between the vorticity and the velocity. One can construct various

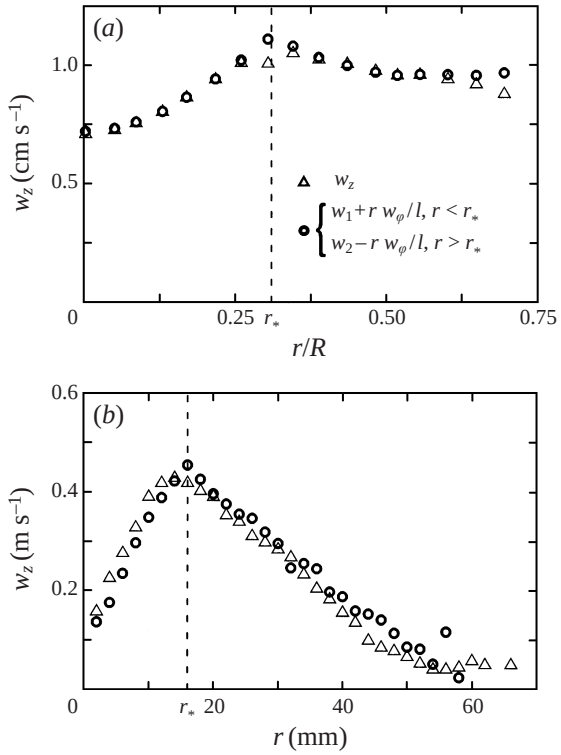

FIGURE 18. Testing of the helical symmetry in a swirl flow with the assumed combination of two vortices: (*a*) data by Brücker & Althaus (1992) $l/R = 0.67$, $w_1 = 0.72$ cm s^{-1}, $w_2 = 1.53$ cm s^{-1}, $r_*/R = 0.31$; (*b*) data by Shtork (1994) $l = 46.7$ mm, $w_1 = 0.12$ m s^{-1}, $w_2 = 0.80$ m s^{-1}, $r_* = 16$ mm, diaphragmed exit orifice, $d_e = 100$ mm, $z_e = 430$ mm, $Re = 2.8 \times 10^4$, $S = 3$, $z = 323$ mm. △, measured values of axial velocity; ○, axial velocity calculated through the measured values of tangential velocity using the condition of helical symmetry.

combinations of the different areas (including non-annular ones) and with a different $\boldsymbol{\omega}$ orientation.

In order to justify theoretically the possibility of combining two vortices let us analyse solution (3.19) for the stream function in the case of an elementary helical filament. If the summand containing w_0 in (3.19) is excluded it is easy to see that the solution is invariant with respect to the sign of l. In essence, w_0 is an integration constant and should be determined separately in each zone. Thus, there is no problem when considering the term with the ratio w_0/l in (3.19). Now we may construct the vortex model combinating areas containing left and right helical filaments (except for the case of intersecting left and right filaments). The above-introduced annular areas are not in contradiction with this requirement.

Using the hypothesis on combining right and left vortices in zones 1 and 2 one can write the resulting relation for testing helical symmetry which connects the tangential and axial velocities (an analogy of relation (3.9) for testing helical symmetry in simple flows) as

$$w_z = \begin{cases} w_1 + rw_\varphi/|l|, & r < r_* \\ w_2 - rw_\varphi/|l|, & r > r_* \end{cases} \equiv w_0 + \frac{r_* w_\varphi(r_*)}{|l|} - \left| \frac{rw_\varphi - r_* w_\varphi(r_*)}{l} \right|. \tag{4.9}$$

Here w_1 and w_2 are the integrating constants.

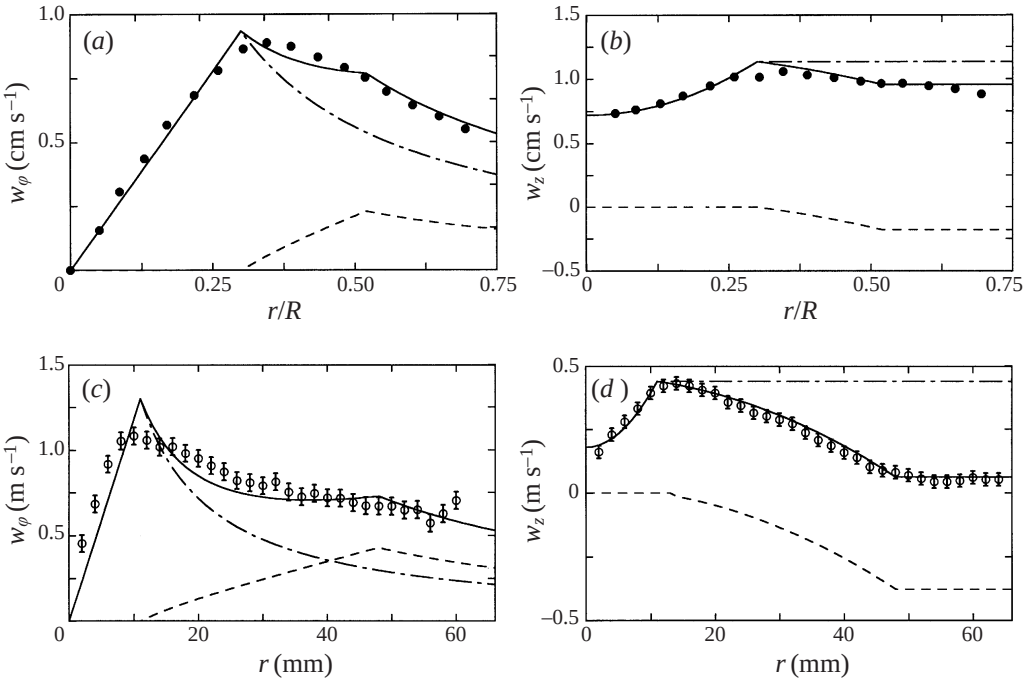

FIGURE 19. Comparison of experimental velocity profiles with exact solution (4.7) for a combination of two vortices. ●, experiment by Brücker & Althaus (1992); ○, experiment by Shtork (1994), data are the same as in figure 18. Calculation by (4.7): - - - , right-handed vortex; -·-·-, left-handed vortex; ——, combined vortex.

It follows from (4.9) that constant w_1 equals w_0 and $w_2 = w_0 + 2r_* w_\varphi(r_*)/|l|$. The last expression follows from the condition of the velocity matching at the boundary of the two zones. Upon the satisfaction of condition (4.9) one can talk about the existence of generalized helical symmetry in the flow with a non-monotonic profile of the axial velocity and respectively about the composition of the two helical vortices.

The results of testing the helical symmetry for the aforementioned regimes are presented in figure 18. These data show that the generalized condition of helical symmetry is confirmed with high accuracy in the experiments by Brücker & Althaus (1992) and here (see figure 16). Because of this we may state that in the regimes described a combined helical vortex occurs.

To approximate the velocity field for these vortices with a rectilinear axis it is apparently sufficient to use the combination shown in figure 17. The velocity field induced in each area is calculated by model I with values of l equal in magnitude and different in sign. The parameters of the basic vortices are chosen so as to reach the best agreement between the computation and the experiment. As is seen from figure 19 the profile of the axial component, w_z, is described very well. The situation with w_φ is worse. This is connected with the fact that the theoretical model at the point of maximum w_φ always has a break since the vorticity at this point undergoes a jump.

Returning to figure 16, note one important feature: the swirl velocity profile does not change with the chamber height whereas the axial velocity profile varies significantly, namely, the velocity maximum is shifted to the vortex axis as the exit orifice is approached. The similarity of the swirl velocity profiles with chamber height

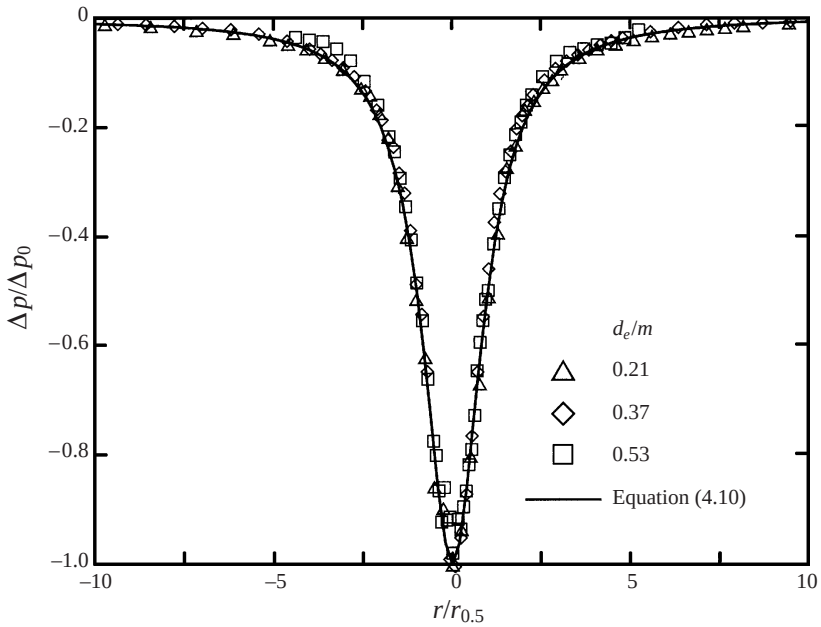

FIGURE 20. Generalization of the bottom pressure profiles for different sizes of the exit orifice. $z_e = 430$ mm, $Re = 2.8 \times 10^4, S = 3$.

was also noted by Escudier *et al.* (1980). This feature also relates to flows with a combination of two vortices. Taking into account that for axisymmetric flow the pressure is determined by a single tangential component of velocity (4.4), one can suggest the possibility of finding the characteristics of the combined vortex by using the data on the bottom pressure as was done for the vortex filaments in § 4.2. Figure 12(*b*) confirms this suggestion. Actually, both for simple vortices and flows with a combination of two vortices the pressure profiles at the bottom and in the flow are identical.

Thus we shall complete our study on flow regimes with the combining of vortices by describing the results of the measurements of the bottom pressure. It can be shown that the pressure data for different diameters of the exit orifice of the chamber are not generalized in the coordinates used in § 4.2. The approach applied to jet flows is found to be acceptable. As the length scale we use the value of the radial coordinate $r_{0.5}$ where the pressure change equals half of the pressure drop p_0. Then the bottom pressure profiles for different d_e generalize well in the coordinates $[\Delta\bar{p} = \Delta p/\Delta p_0,\ \bar{r} = r/r_{0.5}]$ (figure 20). The experimental points are, then, described by model II rewritten in the dimensionless form

$$\Delta\bar{p} = -1/\left(1 + \bar{r}^2\right). \tag{4.10}$$

By this means the hypothesis on the possibility of the appearance of swirl flow regimes with a combination of two vortices allows the description of complex empirical profiles of the radial distribution of the velocity. However, the importance of the combination principle is not only in the approximation of the empirical velocity profiles but also in the possibility of giving a physical interpretation of the flows. Later the principle of combination will be applied to an explanation of the structure of more complicated helical vortices.

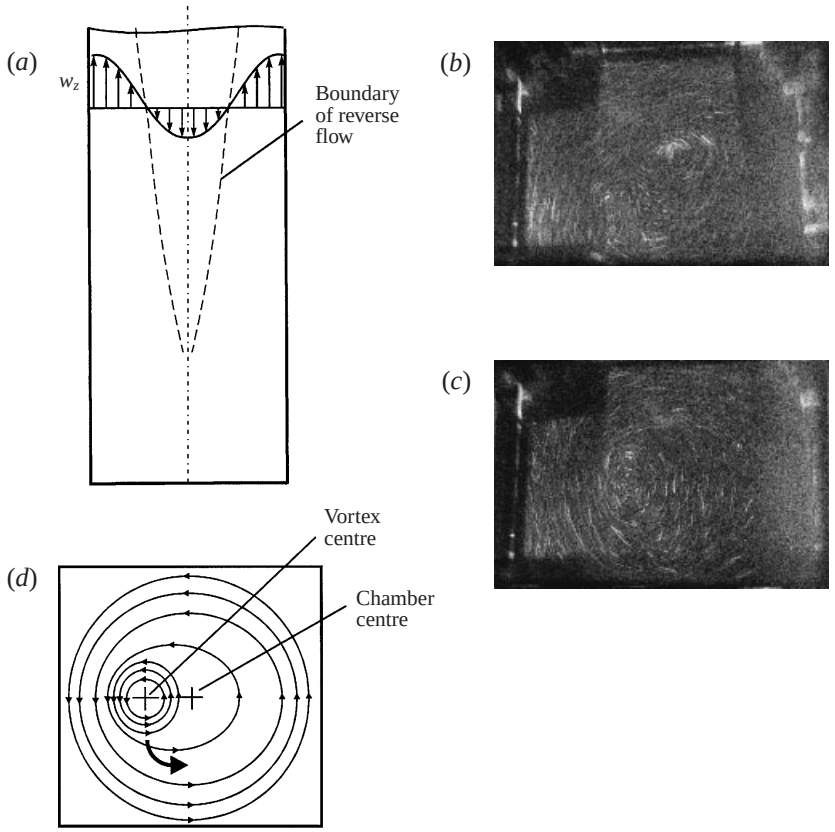

FIGURE 21. Schematics (*a, d*) and visualization (*b, c*) of flow in the vortex chamber with an open exit (diaphragm is absent). (*b, c*) $z = 235$ mm, $Re = 4.3 \times 10^4$, $S = 3$, photographs are taken at different instants in time. One can clearly see the precessing vortex core.

5. Rotating helical vortex

5.1. *Precessing vortex core*

Let us continue a description of flow regimes in the square vortex chamber sketched in figure 1. The further increase in diameter of the exit orifice (up to fully opened) leads to a new significant realignment of the flow. The flow loses its axial symmetry and becomes non-stationary with a pronounced precessing helical vortex (figure 21). The loss of axial symmetry is not related to the location of the side chamber outlet. Furthermore, in this section we shall consider the flow region below the level $z = z_*$ (see figure 1) assuming that the configuration of the exit part of the chamber at $z > z_*$ has no influence on the flow in region $z < z_*$, since the main effect is the existence of a sharp expansion of the flow cross-section at $z = z_*$. Note that the helical symmetry in the flow is conserved as is seen from figure 2(*d*).

In figure 21(*a*), the structure of the swirl flow in a vortex chamber with an open exit is shown schematically. The feature of the flow is the formation of a large near-axis zone of reverse flow with the boundary marked by a dashed line. Also, the maxima of both the axial and the tangential velocity are shifted towards the periphery as follows from the profiles averaged over time. Many works (see Shtym 1985) are devoted to the analysis of flow regimes averaged over time. We are interested, however, in non-stationary (unsteady) phenomena.

As follows from the visual observations, a concentrated extended vortex is formed at the boundary of the zones of upflow and downflow. This vortex rotates together with the flow around the geometric axis of the chamber (see photographs and sketch in figure 21*b*,*c*,*d*) and has a weakly pronounced helical structure. In addition to testing the helical symmetry for mean velocity profiles (figure 2*d*) this also gives grounds for applying the theory of flows with helical symmetry for the description of such regimes.

The rotating concentrated vortices which arise in an unstable swirl flow are usually called precessing vortex cores (PVC). The usual descriptions of PVC are associated with other conditions of the experiment; besides which, the spatial structure of the precessing vortex has not been identified. Kutateladze *et al.* (1987) observed precession of the axis of swirling air flow accompanied by sound generation in a cylindrical channel with a slot tangential supply and an opened exit. Gupta *et al.* (1984) examined the precession in swirlers and swirl burners and analysed the influence of the PVC on combustion. According to Gupta *et al.* (1984) and Sozou & Swithenbank (1969), the precessing vortex core is one of two possible states of swirl flow arising after vortex breakdown. The pattern with the PVC is characterized by the existence of a large near-axis zone of recirculation with a high rate of reverse flow. At the exit of a swirler large-scale three-dimensional disturbances are generated. Combustion strongly affects the PVC. In particular, the amplitude and frequency of the pulsations grow in the flow with combustion of the premixed components (Gupta *et al.* 1984).

In the vortex chamber considered, the most pronounced character of the PVC is observed in the range of angles of nozzle turning $\gamma = 5°$–$10°$ (see figure 1). However, the vortex is not always continuous and stable. Flow visualization in the cross-section of the chamber shows that sometimes two or more vortices are formed which merge thereafter into a single core again. Looking along the air core of the vortex one can see that it is disrupted occasionally into separate parts, which move in a circular path and then merge again into a continuous core.

Data on the precession frequency versus the flow rate are presented in figure 22(*a*,*b*) in dimensional and dimensionless forms for different values of the swirl parameter. The measurements are made by the electrodiffusion probes for velocity, the resistance strain gauge for pressure, and also on the basis of visual observations (in the last case the time period of 100 vortex revolutions was measured with a chronometer and the total error was of the order of 4%). Here f is the frequency of vortex precession, $Sh = fm/w_m$ is the Strouhal number, $Re = w_m m/\nu$ is the Reynolds number, w_m is the mean flow rate velocity, S is the swirl number (see (2.2)). As is seen, the frequency grows linearly with the flow rate. This was also found for other types of swirlers (Chanaud 1965; Cassidy & Falvey 1970). The Strouhal number is self-similar relative to the Reynolds number but depends on the swirl parameter. When $S \leqslant 4$ the Strouhal number increases linearly with S. However, at higher values of S the Strouhal number becomes weakly dependent upon S and has an approximately constant value. Note that the data at large S are not plausible due to the strong instability of the flow and the absence of pronounced PVCs. The existence of a linear relation between f and Q in a wide range of flow rates was the basis for creating vortex flow rate meters.

Many investigators do not identify the PVC with the motion of large-scale vortex structures (helical vortices). Some of them note that the appearance of PVCs is accompanied by the formation of a counterflow along the axis of the swirl flow (Yazdabadi *et al.* 1994). However as was shown in § 3.3, the existence of a counterflow may serve as proof of the generation of a helical structure. The lack of knowledge

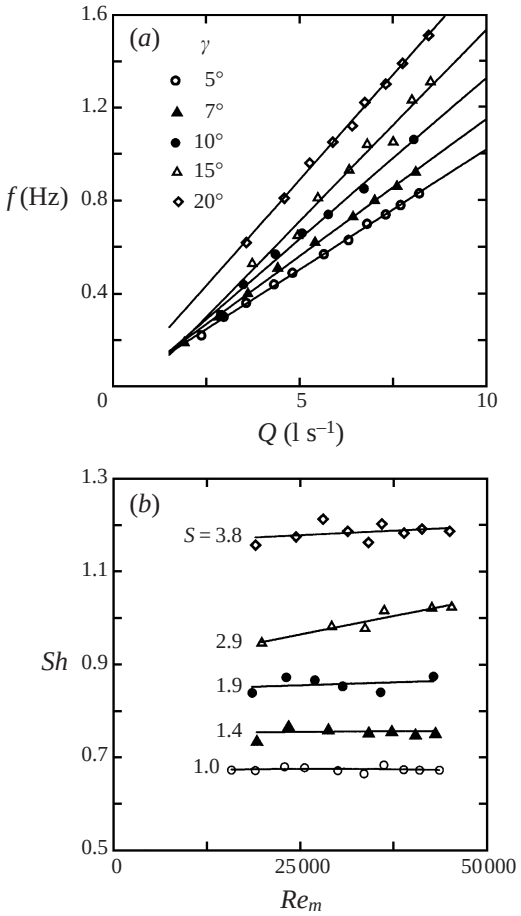

FIGURE 22. Precession frequency versus the flow rate in the dimensional (*a*) and dimensionless (*b*) coordinates.

about the spatial structure of a flow is explained by the complexity of experimentally studying non-steady-state three-dimensional swirl flows (see the review by Alekseenko & Okulov 1996). It is easy to observe the PVC in a plane perpendicular to the flow axis (figure 21). The PVC is seen as a bubbly area moving along the circumference. However, it is difficult to construct the actual spatial geometry of the flow by using the plane pattern. The quantitative flow characteristics are also measured in that plane. Usually the mean velocities and pressure along the radial coordinate are determined. Only Mollenkopf & Raabe (1970) and Yazdabadi *et al.* (1994) obtained distributions for the velocity components over the entire cross-section using the technique of phase averaging. Such results make it possible to establish the precession frequency and the existence of a reverse flow rather than the spatial flow structure.

5.2. *Helical vortex with finite-size core*

The solution constructed in § 3.3 is not really acceptable for the theoretical description of rotating helical vortices since the self-induced velocity of an infinitely thin filament equals infinity. In reality, the vortex core always has a finite size. In accordance

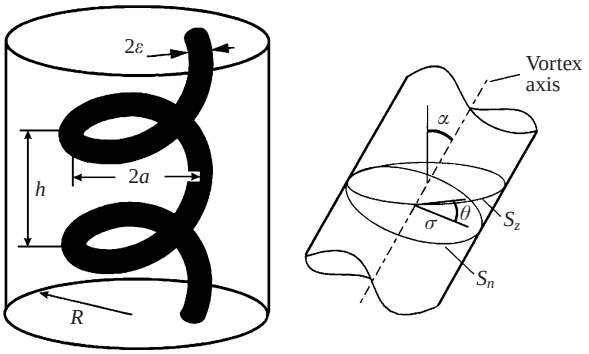

FIGURE 23. Model of a helical vortex with a finite size core.
The local coordinate system also is shown.

with this, let us construct a model of a vortex having a helix-like core with a round cross-section of radius in a plane perpendicular to the vortex axis (figure 23). We consider the simplest distribution of vorticity to satisfy the Helmholtz equation (3.12), i.e. $\omega_z = \text{const}$ within the core. The velocity field induced by such a vortex may easily be represented through solution (3.20) assuming that the vortex is the superposition of infinitely thin vortex filaments uniformly distributed within the vortex core. Note that vorticity modulus, ω, is not constant because the vortex filaments in such a vortex are entangled and the inclination of the vorticity vector varies over the vortex cross-section. Actually, it follows from the geometric construction that

$$\omega_z = \omega l / \left(l^2 + r'^2\right)^{1/2}.$$

Here r' is the radial coordinate of the vortex filament. It is seen that at $\omega_z = \text{const}$ and $l = \text{const}$ the value of ω grows with distance r'.

We represent solution (3.20) for an infinitely thin helical vortex filament with circulation Γ as $\boldsymbol{w} = \Gamma \boldsymbol{F}$, where $\boldsymbol{F}$ is a function of the filament geometry only. For the continuous distribution of vortex filaments we can write for a thin vortex tube the differential relation

$$\mathrm{d}\boldsymbol{w}_\varepsilon = \boldsymbol{F}\,\mathrm{d}\Gamma,$$

where $\boldsymbol{F}$ is the same function as for an infinitely thin vortex filament, $\mathrm{d}\Gamma$ is the circulation of the separated vortex tube with cross-sectional area $\mathrm{d}s_n$, subscript ε means the solution for the vortex with core radius ε. It is more convenient to seek a solution for the horizontal section ($z = 0$) of the vortex tube with area s_z. We have from the Stokes theorem

$$\mathrm{d}\Gamma = \boldsymbol{\omega}\,\boldsymbol{n}\,\mathrm{d}s_n = \omega\,\mathrm{d}s_n = \omega_z \mathrm{d}s_z.$$

From this it follows that $\Gamma = \omega_z s_z$, emphasizing that Γ is the circulation in a helical vortex with a finite size core. The area of the cross-section of the helical vortex in the horizontal plane is

$$s_z = \int_{s_n} \frac{\left(l^2 + r'^2\right)^{1/2}}{l}\,\mathrm{d}s_n.$$

In the light of these relations we can obtain an equation for the determination of the

velocity induced by a helical vortex with a finite-sized core:

$$\boldsymbol{w}_\varepsilon(r,\varphi,z) = \int \boldsymbol{F}\,\mathrm{d}\Gamma = \int \omega_z \boldsymbol{F}\,\mathrm{d}s_z = \frac{\Gamma}{s_z}\int \boldsymbol{F}\,\mathrm{d}s_z$$
$$= \frac{1}{ls_z}\int_0^{\varepsilon}\int_0^{2\pi} \left(l^2 + r'^2\right)^{1/2} \boldsymbol{F}(r,\varphi,z;r',\varphi',z')\,\sigma\,\mathrm{d}\sigma\,\mathrm{d}\theta. \tag{5.1}$$

The integration is done over the circle of radius ε with its centre at $r' = a$, $\varphi' = \varphi_0$, $z' = 0$ (figure 23). The local polar coordinates σ, θ with their centre at point (a, φ_0, 0) are connected with the coordinates of the basic cylindrical coordinate system r', φ', z' by the relations

$$r'\cos(\varphi' - \varphi_0) = a + \sigma\cos\theta,$$
$$r'\sin(\varphi' - \varphi_0) = \sigma\sin\theta\,\cos\alpha,$$
$$z' = -\sigma\sin\theta\,\sin\alpha,$$

where α is the angle between the vortex axis and the z-axis ($\tan\alpha = a/l$).

To examine the possibility of describing actual flows by using the above approximate model, we shall compare the calculations according to (5.1) with the experimental data. As is noted in the previous section most experimental data for rotating helical vortices represent averaged flow characteristics at a fixed point of the radial coordinate. Taking into account the rotation of helical vortices, averaging over time may be replaced by averaging over the angular coordinate φ. We find the mean velocities for model (5.1) using this method as

$$\langle \boldsymbol{w}_\varepsilon \rangle = \frac{1}{2\pi}\int_0^{2\pi} \boldsymbol{w}_\varepsilon\,\mathrm{d}\varphi. \tag{5.2}$$

Substitute (5.1) into (5.2) and change the sequence of integration. Allowing for integrals of the series involved in solution (3.20) being zero we reduce the task of finding averaged velocities to the calculation of the integral $F(r)$:

$$\langle w_{r\varepsilon}\rangle \equiv 0, \quad \langle w_{\varphi\varepsilon}\rangle = \frac{\Gamma}{2\pi r}F(r), \quad \langle w_{z\varepsilon}\rangle = w_0 - \frac{\Gamma}{2\pi l}F(r),$$
$$F(r) = \frac{1}{S_{cz}}\int_{S_{cz}} \begin{Bmatrix} 0, & r < r' \\ 1, & r \geqslant r' \end{Bmatrix} \mathrm{d}S'. \tag{5.3}$$

Here S_{cz} is the area of the cross-section of the core with plane $z = \text{const}$. The integral in (5.3) equals the area of the intersection of a circle of radius r with cross-section S_{cz}. The ratio of the areas in (5.3) does not vary if both figures are projected on the plane perpendicular to the helical vortex axis. By this means we find that $F(r) = S^{(0)}/\pi\varepsilon^2$ where $S^{(0)}$ is the area of the intersection of circle $\sigma = \varepsilon$ with the ellipse given by formula

$$(a + \sigma\cos\theta)^2/l^2 + (\sigma\sin\theta)^2/(a^2 + l^2) = \sigma^2.$$

Returning to the aim announced previously let us estimate the value of model (5.1) or its consequence (5.3) to the description of bounded intensively swirling flows. For this purpose we shall compare the calculations according to formula (5.3) with the experimental data on tangential and axial velocity distributions in various vortex chambers. Figure 24(a) presents the velocity profiles in a cylindrical chamber with a tangential swirler and closed front endwall (Kutateladze *et al.* 1987). The data for our chamber with a square cross-section and an open exit are shown in figure 24(b). All flows are characterized by the formation of a precessing vortex structure. Only the

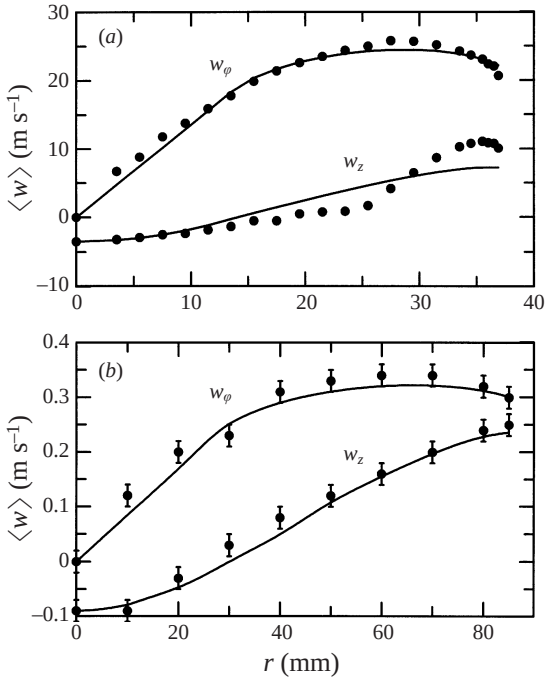

FIGURE 24. Averaged velocity profiles in a swirl flow with a precessing vortex core: ——, calculation by formula (5.3) for a rotating helical vortex; ●, experiment. (*a*) Kutateladze *et al.* 1987 (near-wall swirl jet in a channel with a closed endwall, $x = 175$ mm); (*b*) measured data (tangential nozzle swirler, chamber without diaphragm, $Re = 3.2 \times 10^4$, $S = 1$, $z = 63$ mm).

mean flow characteristics were measured. Because of this (5.3) is used for comparison. Necessary parameters of vortex structures have the values, respectively:

$$\Gamma = 5.15 \text{ m}^2 \text{ s}^{-1}; \; l = -0.076 \text{ m}; \; a = 0.011 \text{ m}; \; \varepsilon = 0.025 \text{ m}; \; w_0 = -3.5 \text{ m s}^{-1}$$

and

$$\Gamma = 0.16 \text{ m}^2 \text{ s}^{-1}; \; l = -0.078 \text{ m}; \; a = 0.028 \text{ m}; \; \varepsilon = 0.057 \text{ m}; \; w_0 = -0.09 \text{ m s}^{-1}.$$

One can draw the following conclusions on the basis of the comparison: the proposed model describes the experiment well even for ε of the order of a or l; in the various apparatuses, swirl flows of similar structure are formed which may be represented through superposition of translational and pure helical motions in accordance with (3.9).

5.3. *Precession frequency*

The exact solution for the velocity field induced by a helical vortex filament in a tube (see § 3.3) permits the stricter derivation of a formula for the angular velocity of vortex rotation in a tube.

The first result for the angular frequency of the helical disturbances travelling round the original vortex, Ω, in the long-wave ($l/a \gg 1$), small-amplitude ($a/\varepsilon \ll 1$) limit was obtained by Kelvin (1880)

$$-\hat{\Omega} = -\Omega \frac{4\pi l^2}{\Gamma} = \ln \frac{2l}{\varepsilon} + \tfrac{1}{4} - E. \tag{5.4}$$

Here $E = 0.5772...$ is Euler's constant. Moore & Saffman (1972) generalized this

result for vortices with arbitrary distribution of the swirl and axial velocities inside the core. Their formula has received good confirmation in experiments by Maxworthy *et al.* (1985). Based on Moore & Saffman's (1972) analysis, Ricca (1994) showed that the result (5.4) would be the same for an arbitrary helix of large pitch. Nonetheless, he compared calculations of the terms responsible for the non-local induction made with the use of Hardin's (1982) formulas and another representation of the right-hand side of (5.4):

$$\ln \frac{1}{\kappa\varepsilon} + C, \qquad C = -\ln \frac{l}{a} + \tfrac{1}{4} + \ln 2 - E, \tag{5.5}$$

where $\kappa = a/(a^2+l^2)$ is the curvature of the helix. Though the asymptotics at $l/a \gg 1$ are identical, the formula (5.5) describes the computational data better with a moderate helix pitch. The behaviour of C with a small helix pitch was analysed by Kuibin & Okulov (1998):

$$C = \frac{a}{l} + \ln \frac{l}{a} + \tfrac{3}{4}, \qquad l/a \ll 1$$

Our aim is to determine the wall influence on the motion of a helical vortex in a cylindrical tube. To do this we find the contribution of the tube wall to the motion velocity at the point $[r = a, \chi = \chi_0]$ with the help of (3.24). As only the binormal velocity component,

$$w_b = B_a(w_z a/l - w_\varphi) = -B_a w_\chi, \tag{5.6}$$

is responsible for the motion of the vortex, we have

$$-\hat{\Omega} = \hat{w}_b = \ln \frac{1}{\kappa\varepsilon} + C + \hat{w}_b^{(R)}, \qquad \hat{w}_b^{(R)} = -\frac{4l}{aB_a^3}\left(S_\chi^{(R)} + R_\chi^{(R)}\right). \tag{5.7}$$

Here $B_a^2 = l^2/(a^2+l^2)$, $\hat{w}_b = 4\pi w_b/\Gamma\kappa$ is the normalized velocity, superscript (R) relates to the terms in (3.25)–(3.26) responsible for the interaction with the wall. In addition to the separation of the polar singularity made in (3.25)–(3.26) we separate the logarithm from $R_\chi^{(R)}$ in a manner similar to the separation of the logarithm in a stream function. The result is

$$\hat{w}_b^{(R)} = \frac{2l^2}{B_a^3 a^2}\left[k \ln \frac{\tilde{R}^2 - \tilde{a}^2}{\tilde{R}^2} - \frac{\tilde{a}^2}{\tilde{R}^2 - \tilde{a}^2}\right], \tag{5.8}$$

where $k = (9B_R - 7B_R^3 - 3B_a + B_a^3)/12$, $\quad B_R^2 = l^2/(R^2+l^2)$.

The quantities denoted by a tilde correspond to the distorted distances introduced in (3.22). The remainder in $R_\chi^{(R)}$ after the separation of the logarithm does not exceed 1.5% and it is neglected in (5.8).

Note that it is necessary to take into account the velocity at the axis if we consider vortex motion in a tube. In the case of a vortex in an unbounded space $w_0 = \Gamma/2\pi l$. The contribution of the dimensionless parameter $\beta = w_0 2\pi l/\Gamma$ to the binormal component follows from (3.24):

$$\hat{w}_b^{(\circ)} = 2(\beta - 1)/B_a. \tag{5.9}$$

Considering $\hat{w}_b^{(R)}$ and $\hat{w}_b^{(\circ)}$ as additions to C in (5.5) let us evaluate their contribution with the help of formulae (5.8) and (5.9). Figure 25 shows the dependence of C on the dimensionless pitch of the vortex for the case of $\beta = 1$. Note that $C = C(l/a, a/R, \beta)$ where l/a is the same as the dimensionless torsion used by Ricca (1994). The first curve calculated at $a/R = 0$ (i.e. $R \to \infty$) corresponds to the case considered by him. With the increase in a/R the dependence departs from the logarithmic law and tends

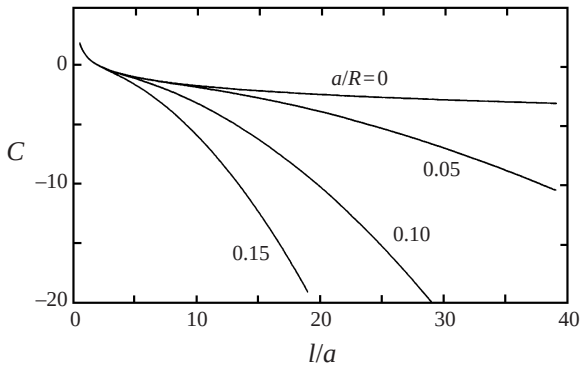

FIGURE 25. Constant C in the expression (5.5) for the binormal velocity of the helical vortex versus the dimensionless helix pitch ($\beta = 1$).

towards a parabolic asymptote at high values of l/a and l/R:

$$C \to -2l^2/(R^2 - a^2).$$

The influence of β is limited to an almost parallel shift of the curves along the vertical since the growth of l/a leads to the fast approach of the respective term to the asymptotic value $2(\beta - 1)$.

The total binormal velocity may be found by summing (5.5), (5.7)–(5.9):

$$\hat{w}_b = \ln\frac{1}{\kappa\varepsilon} + \left(\ln\frac{2a}{l} + \tfrac{1}{4} - E\right) + \frac{2l^2}{B_a^3 a^2}\left[k\ln\frac{\tilde{R}^2 - \tilde{a}^2}{\tilde{R}^2} - \frac{\tilde{a}^2}{\tilde{R}^2 - \tilde{a}^2}\right] + \frac{2(\beta - 1)}{B_a}. \quad (5.10)$$

Now let us determine the angular velocity, n, of the rotation of a helical vortex. In view of (3.1), (3.8) and (5.6) we derive $n = w_\varphi/a = B_a(w_0 B_a/l - w_b/a)$.

Moving now to the phenomenon of vortex core precession let us note that the precession frequency f is considered to be the frequency at which the vorticity spot passes near a fixed point (probe) on a tube wall. This is the frequency of rotation of the vortex core in a fixed plane and the angular frequency, $2\pi f$, does not coincide with the angular velocity n of the vortex rotation. Such a discrepancy is explained by the fact that the spiral vortex has non-zero axial velocity w_0. Owing to the helix-like structure of the vortex, even its pure displacement along the z-axis at $n = 0$ leads to the rotation of its core in a fixed plane perpendicular to the z-axis.

Taking into account the above notation and the connection between the axial and tangential velocities in flow with the helical symmetry (3.9), the precession frequency of a vortex core may be expressed as

$$f = \frac{1}{2\pi}\left(\frac{n}{B_a^2} - \frac{w_0}{l}\right) = -\frac{w_b}{2\pi a B_a} = -\frac{\Gamma}{8\pi^2 a^2}\frac{a^2}{l^2}B_a\hat{w}_b. \quad (5.11)$$

We split the frequency into four parts in accordance with the four terms in the right-hand side of (5.10): $f = f_\kappa + f_\tau + f_R + f_{w_0}$. The first term is determined by the size of the vortex core and curvature of the axis. The second term is responsible for the influence of the axis torsion. The third term is the contribution due to the wall. The last term reflects the effect of the uniform flow; this contribution is clear and is proportional to w_0/l (or β/l^2).

The dependence of the dimensionless precession frequency, $\bar{f} = 8\pi^2 a^2 f/\Gamma$, on a/l is presented in figure 26 for different values of R/a ($\varepsilon/a = 0.3$, $\beta = 1$, the solid lines).

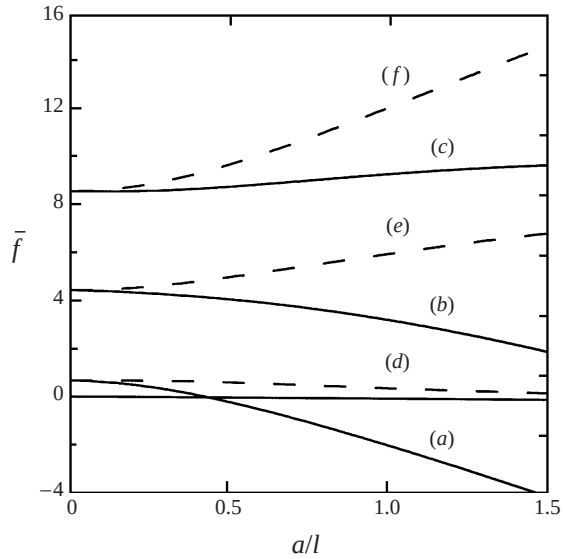

FIGURE 26. The dependencies of the vortex precession frequency (——) and the constituent corresponding to the wall influence (- - -) on the quantity a/l ($\beta = 1, \varepsilon/R = 0.05$). $(a, d)\, a/R = 0.5$; $(b, e)\, a/R = 0.83$; $(c, f)\, a/R = 0.9$.

The negative frequency means that the vortex moves in a direction contrary to the flow rotation. The dashed lines correspond to the contribution of the wall effect to the frequency. The wall's greatest influence takes place when the vortex is located near the wall (curves *c, f*). When the vortex size a is half of the tube radius the effect is quite weak (curves *a, d*), because R enters (5.10) in squared form.

It follows from (5.11) and (5.10) that in the long-wave approximation

$$f\,|_{l\gg a} = \frac{\Gamma}{4\pi^2 a^2}\left[\frac{a^2}{R^2-a^2} - \frac{a^2}{2l^2}\left(2\beta - 1 + \frac{R^2}{a^2}\ln\left(1-\frac{a^2}{R^2}\right) - \frac{2a^2}{R^2} + \ln\frac{2l}{\varepsilon}\right) + O\left(\frac{a^4}{l^4}\ln\frac{l}{a}\right)\right]$$

and in the limit $l \to \infty$ we obtain the well-known formula for the motion frequency of a point vortex in a circular area (Lamb 1932). The points corresponding to this limit are the points of intersection of the curves with the ordinate.

Strictly speaking, expression (5.10) is valid either for slender helical vortex filaments or for weakly curved columnar vortices. Its derivation was made by assuming a simple model of vorticity distribution in a core: $\omega_z = \text{const}$. Nonetheless we shall try to compare the calculated frequency with the known experimental data. The frequency for the case presented in figure 24(*a*) reported by Kutateladze *et al.* (1987) was 100 Hz. The calculation according to formula (5.11) with the parameters found in § 5.2 and with $R = 0.0375$ m yields $f_c = 98.8$ Hz. For the vortex precession in our vortex chamber (see figure 24*b*) the measured frequency is $f = 0.6 \pm 0.024$ Hz and the corresponding calculated value is $f_c = 0.585$ Hz.

An analysis of formula (5.10) permits us to draw one more important conclusion. It concerns the possibility of stationary (immobile) helix-like vortex structures when the self-induced velocity of rotation of a helical vortex caused by its curvature and torsion (first and second terms in right-hand side) is compensated by the wall-induced

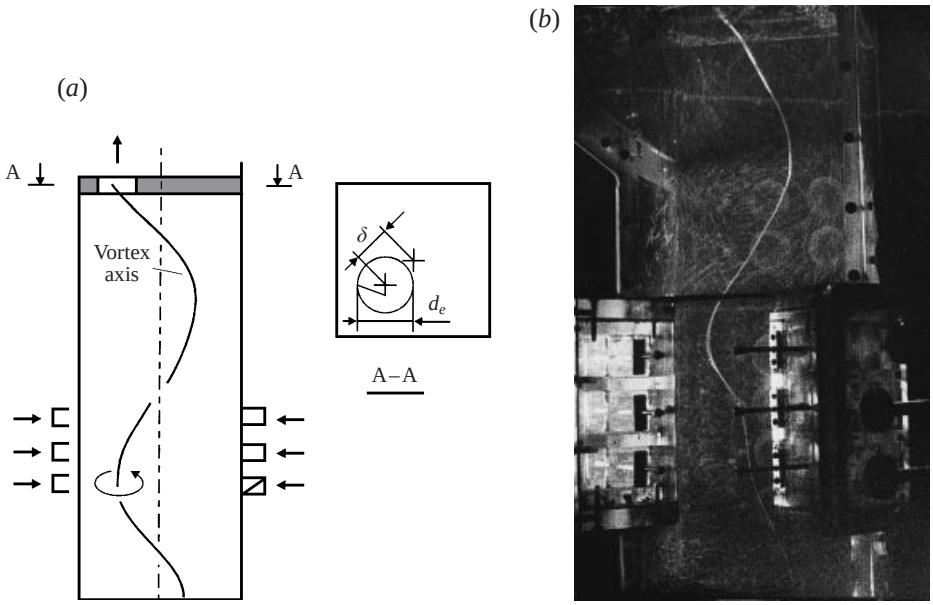

FIGURE 27. Schematic (*a*) and visualization (*b*) of a swirl flow with a left-handed helical vortex. $d_e = 70$ mm, $z_e = 560$ mm, $\delta = 62$ mm, $Re = 2.4 \times 10^4$, $S = 4.5$. Such a vortex is generated due to the shifted exit orifice.

velocity (third term) and by the pure translational motion. The results of studying such vortices will be described in the next section.

6. Stationary helical vortex filaments

As is noted in the previous section, flow regimes are possible where the vortex rotation is compensated by the mean motion of the medium in the channel. In such cases stationary helical structures may appear which were actually observed for the first time in our experiments.

The helical vortices may arise either due to the instability of the axisymmetric flow to spiral modes or as a result of the deformation of the rectilinear vortex filament by means of an artificial distortion of the boundary conditions. In the first case the spiral vortices are non-stationary and predominantly three-dimensional (spiral waves, spiral vortex breakdown). Here we are concerned only with the second method of generating helical vortices that allows us to observe stationary (immobile) structures.

6.1. *Single helical vortices*

As in the previous sections, the flow in the vortex chamber is curled on the right and a diaphragm with an orifice of diameter d_e is placed in the exit section. The central location of the orifice leads to the formation of a stable rectilinear vortex (vortex filament). The displacement of the exit orifice by distance δ relative to the chamber axis causes a drastic change in the flow structure (figure 27). The air filament, which visualizes the vortex core, curves into a spiral. As a whole this structure is immobile. As this takes place, the liquid particles move around the spiral axis making a double spiral motion. In the vicinity of the geometrical chamber axis, the liquid velocity is small and directed downwards although an intense flow is observed along the axis of

the vortex filament towards the exit orifice. The direction of the vortex axis screwing is opposite to the particle motion, i.e. a left-handed vortex is formed. The maximum displacement of the air filament from the chamber axis grows by increasing the displacement of the exit orifice and achieves 43% of half the width of the chamber, which testifies to the nonlinearity of the flow perturbation. It is necessary to note that in such a complex and turbulent flow (Re achieves 4×10^4) an extremely thin air filament remains continuous. In particular, this fact may be related to the decay of the turbulence near the axis of an intense vortex.

The formation of the spiral shape of the rotation axis is observed at all angles of nozzle turning $\gamma > 5°$. However, the most stable state of an air filament is realized at some intermediate position of the nozzles: $\gamma = 10°$–$20°$.

In other cases the periodic breakdown of the air filament occurs due to small-scale disturbances. The shape of the exit orifice has no practical influence on the flow pattern (in particular, with a slot in place of the round orifice on the retention of the area). The displacement of the diaphragm orifice leads to some shifting of the point where the vortex axis touches the channel bottom, however, by no more than 10–20 mm.

The helical shape that arises during the deformation of a vortex filament is explained well by the self-induced motion. Also the immobility of a helical structure may be explained correspondingly as a consequence of the compensation of the helix rotation by the mean flow in a bounded space. Nonetheless the question remains why the vortex axis is screwed to the left but not to the right. A reasonable explanation follows from the analysis of the exact solution for velocity field (3.20). Actually, the left-handed helical filament leads to the decay of the axial flow in the near-axis zone of the chamber. This is clearly seen in figure 8. Indeed, in our case, the displacement of an orifice excludes the possibility of flowing along the geometrical axis of the chamber (or helical structure). By this means a regime with a left-screwing vortex axis is realized.

On the other hand, the theory predicts that in the case of a right-hand helical vortex the intense stream along the geometric axis of the chamber (helical structure) and its decay at the periphery (see, in particular, figures 6, 8) exist. Because of this, the assumption was made that in the experiment, the right-hand vortex could appear in the chamber with a centrally located exit orifice (to organize the flow along the chamber axis) and an inclined bottom (to cause initial deformation of the vortex axis). Actually, such a right-handed structure was immediately found at these conditions as is clearly demonstrated in figure 28.

One can state in the framework of the proposed theoretical model that, in the initial combined vortex, the right-handed helical vortex is suppressed in the first case and the left-hand vortex is excluded in the second case.

The above analysis permits us to suggest a hypothesis about the existence of more complex helix-like vortex structures with the transition from a right-handed to a left-handed symmetry. The hypothesis was tested by modifying the set-up to change the inclination of the chamber bottom during the experiment. At the chamber exit the diaphragm was set with an orifice of diameter $d_e = 70$ mm, shifted from the centre by 62 mm. A well-defined stationary (immobile) vortex structure with a transition from a right helical symmetry to a left one was found under the following conditions: the angle of the bottom inclination to the horizontal $\beta_b = 20°$; the flow rate $Q = 5.25$ l s^{-1}; the geometrical swirl parameter $S = 3$. Figure 29 presents photographs of the thin air filaments that fix the geometry of the vortex axis. Photographs of the same immobile vortex were taken from two directions at an angle of 90°. The different number of

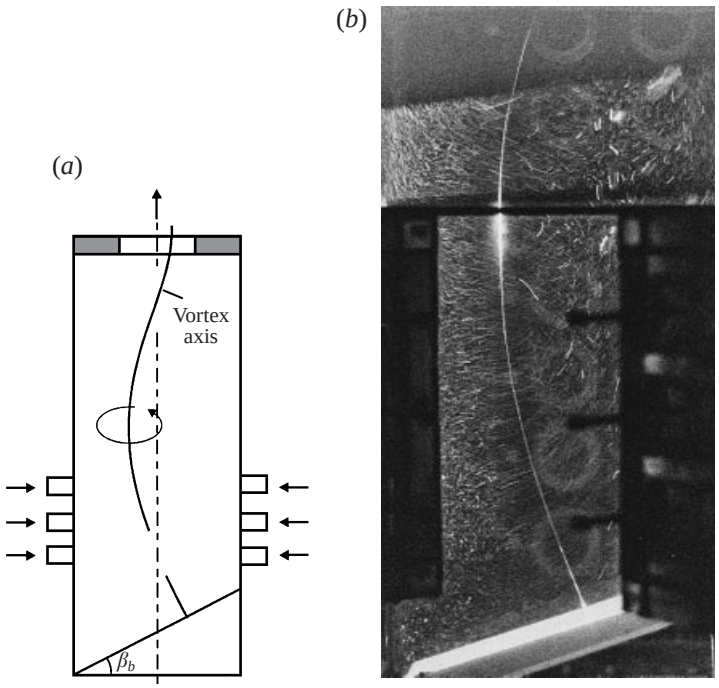

FIGURE 28. Schematic (*a*) and visualization (*b*) of a swirl flow with a right-handed helical vortex. $d_e = 70$ mm, $z_e = 390$ mm, $\beta_b = 18°$, $Re = 1.3 \times 10^4$, $S = 2.9$. Such a vortex is generated due to the inclined bottom.

turns in the photographs is explained by the changing direction of helix screwing in the vortex (see sketch in figure 29). In the lower part of the chamber the right-hand helical vortex is realized and a vortex with left helical symmetry is observed in the upper section of the chamber. The transition region in the centre has a smooth character. Here the helical symmetry breaks down similarly to the case of touching the left vortex with the horizontal plane.

6.2. *Double helix*

The above-described experimental observations of helical structures concern single vortex filaments. However, the theory of helical vortices (see § 3.3) allows for the existence of an arbitrary number of interacting helical vortex filaments. One could state *a priori* that the experimental observation of such phenomena must be extremely difficult: there is little evidence to prove the existence of double spiral structures (non-stationary and non-uniform). Chandrsuda *et al.* (1978) detected the spiral binding of two extended vortices in a boundary layer. Boubnov & Golitsyn (1986) observed the unsteady spiral coupling of two vortex filaments in a state of free convection in a rotating vessel, the final stage being the merging of the two vortices into a stronger one. The system of interacting hairpin vortices in the wake behind a body in a boundary layer (Acarlar & Smith 1987) and in the jets (Perry & Lim 1978) is apparently bi-spiral. The double spiral emerges also in vortex breakdown (Faler & Leibovich 1977), but it is not evident in this case that the coloured jets are the vortex axes.

The interaction of vortex filaments seems to play a principal role in hydrodynamics. It is supposed (Takaki & Hussain 1984) that spiral coupling is the elementary interaction in turbulence.

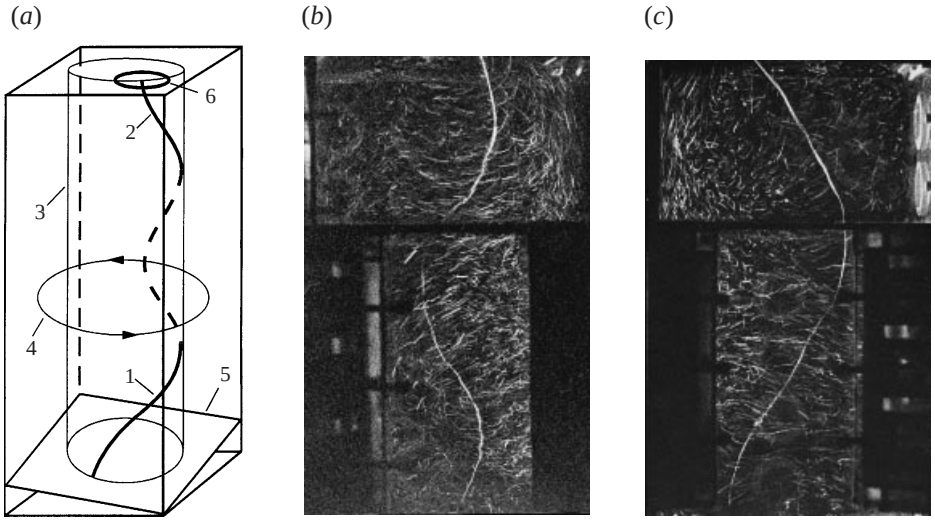

FIGURE 29. Immobile helical vortex with changing helical symmetry. (*a*) Diagram of flow: 1, right-handed vortex; 2, left-handed vortex; 3, imaginary cylindrical surface; 4, direction of flow swirling; 5, inclined bottom; 6, shifted exit orifice. (*b, c*) Flow visualization; photographs are taken from two directions at an angle of 90°. $d_e = 70$ mm, $z_e = 420$ mm, $\delta = 62$ mm, inclination angle of the bottom $\beta_b = 20°$, $Re = 2.8 \times 10^4$, $S = 3$.

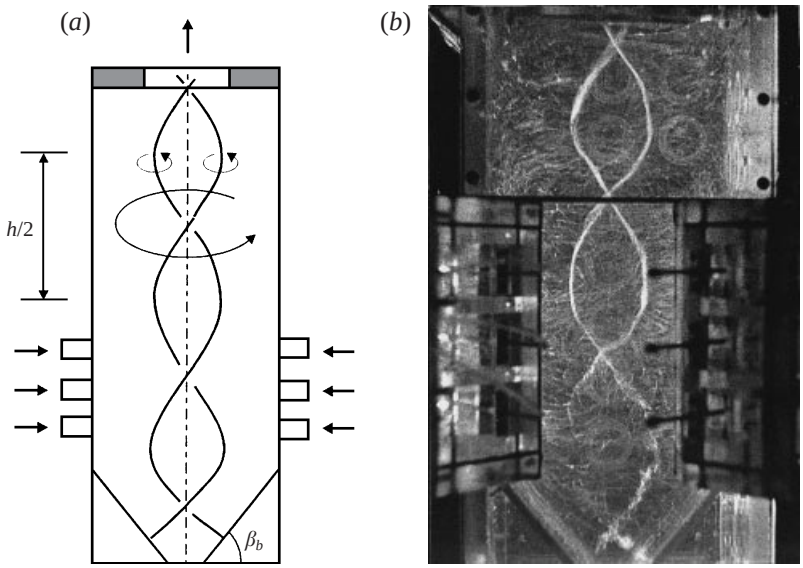

FIGURE 30. Schematic (*a*) and visualization (*b*) of flow with a double helix. $d_e = 65$ mm, $z_e = 420$ mm, $\beta_b = 50°$, $Re = 4 \times 10^4$, $S = 3$. Such a regime is formed due to the existence of two slopes on the chamber bottom.

Attempts to generate stationary double helixes were made by authors after the observation of stable single helical filaments, using the trial-and-error method (Alekseenko & Shtork 1992).

It was found that a double helix arises in a vortex chamber with a centrally located exit orifice and two plane slopes in the channel bottom (figure 30). A double helix represents two entangled helical vortex filaments of the same sign. The filament

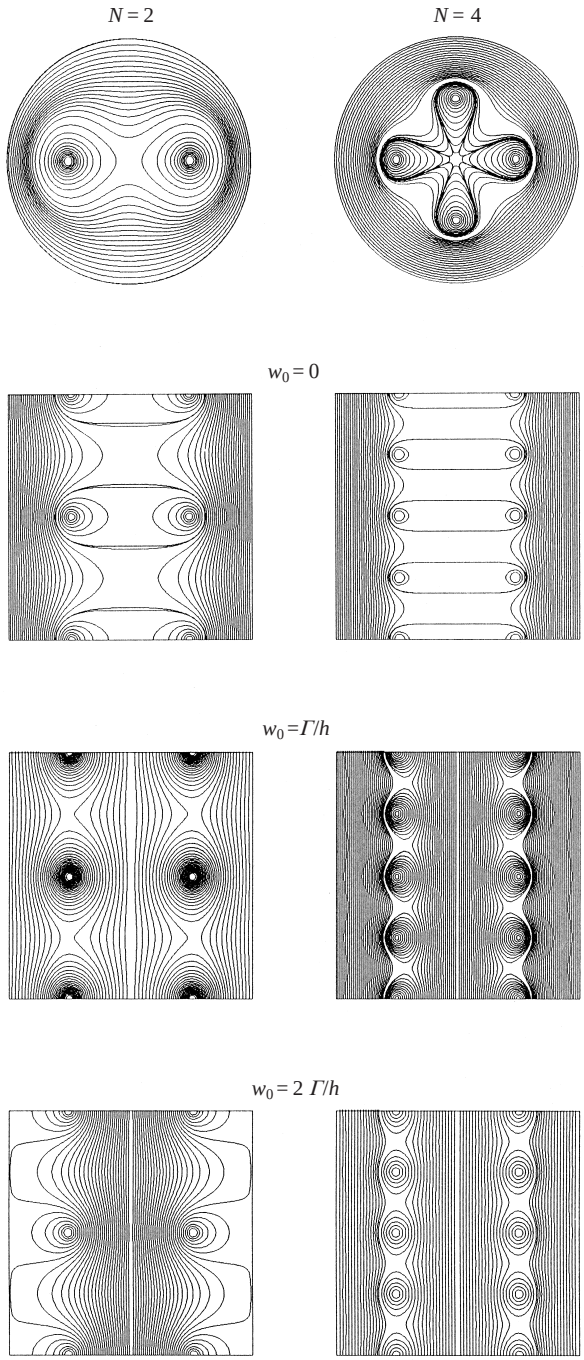

FIGURE 31. Multivortex structures in a cylindrical tube (calculation). N is the number of infinitely thin helical vortex filaments.

screwing corresponds to the direction of flow swirling, i.e. these are right-handed helical vortices. Now, it is understood on the basis of the theoretical model developed that the screwing of vortex axes to the right is caused by the central location of the exit orifice (that allows intensive flow along the chamber axis). As in the case

of a single right-handed vortex the existence of two inclined slopes on the bottom is related to the necessity of forming an initial distortion of the vortex axes. The observed kinematics of the velocity field (by the trajectories of the air bubbles) corresponds completely to the theoretical calculations (see figure 31, number of vortices $N = 2$).

Contrary to the relatively stable one-spiral vortex flow the bi-spiral regime should be considered to be quasi-stationary for the following reasons. First, the air lines, which visualize the vortex axes, are not ideal lines. They oscillate randomly and may break sometimes. Secondly, one of the filaments always tries to dominate, since, in order to detect a double helix, fine adjustment of the nozzle position and sometimes of the flow rates through separate nozzles is required. But in general, the bi-spiral regime of the vortex motion is observed clearly. The Reynolds number, as in other experiments, does not significantly influence the flow patterns.

The parameters of the double helix (distance $2a$ between the filaments, helix pitch h and number j of half-waves) depend essentially on the inclination angle β_b of the slopes on the chamber bottom. For example, $j = 3$, $h = 250$ mm, $2a = 60$ mm for $\beta_b = 50^\circ$ (figure 30) and $j = 6$, $h = 115$ mm, $2a = 25$ mm for $\beta_b = 30^\circ$.

The theoretical model allows for an arbitrary number of helical vortices in a multivortex structure. An example of a streamline picture for four vortices is shown in figure 31 ($N = 4$). However, in the experiment, the observation of structures including more than two vortices is hampered by their instability arising during vortex interactions leading to breakdown and (or) merger. Besides which, the formation of several vortices instead of a unit means that their strength decreases by several times. For these reasons, our experiments did not allow the emergence of a system consisting of four well-defined vortices (which is most probable in a square chamber). In order to generate four vortices, the bottom was made in the form of four steps with inclined upper surfaces. In the vicinity of such a bottom, four vortices were observed clearly. However, they were almost always disrupted in the flow core and could be seen only for short intervals of time. The characteristic of the four-vortex pattern is that the vortices are weakly curved and weakly pronounced. On the other hand, the intensive flow along the chamber axis is marked. This description correlates well with the computed flow pattern for a four-vortex structure.

7. Conclusions

Helical vortices in a swirl flow bounded by solid walls have been studied theoretically and experimentally.

A theoretical model of the helical vortices has been developed, which is based on the Euler equations and the assumption of the helical symmetry of the flow. The two-dimensional linear differential equation in partial derivatives for the stream function (3.13) has been derived. Pitch l and velocity w_0 at the flow axis are the parameters of the problem. Unlike the previous treatments, swirl flow is examined in a bounded space – a cylindrical tube. The main assumption of the theoretical model is that the hypothesis of helical symmetry has been carefully tested.

The exact analytical solution for an infinitely thin helical vortex filament is the initial result of the theory. The expressions for the stream function and the velocity components are written in the form of an infinite series of cylindrical functions (formulae (3.19)–(3.20)). They are presented through singular parts and regular remainders. The regular remainders are small in a wide range of parameters and often they may be

neglected. The singular parts are written through the elementary functions (formulae (3.22), (3.25)).

On the basis of the solutions obtained, a detailed analysis has been performed on the velocity field induced by one or several infinitely thin helical vortex filaments in a tube for a wide range of parameters (the pitch and radius of the helix, the tube radius, the velocity at the tube axis, the number of vortex filaments). It is necessary to underline the following fundamental result. The right-handed helical filament (the vortex axis screwed along the direction of flow swirling) induces intensive flowing along the geometrical axis of the tube, but moderates the axial motion at the periphery. The left-hand vortex leads to the opposite effect. These phenomena give one the possibility of explaining the experimental observations of helical vortices with different helical symmetry.

An infinitely thin vortex filament is an idealization. In real fluid, the vortices have a core of finite size and such vortices may be adequately modelled by the continuous distribution of vortex filaments. The axisymmetric (or columnar) vortex is a widespread one. However, contrary to the commonly accepted representations, the vortex core is assumed to be filled with helical vortex filaments but not rectilinear ones! Therefore the vorticity vector is directed at some angle to the z-axis and as a consequence axial motion is generated. The three simplest vorticity distributions are considered: step, hat and Gaussian ones. For circumferential velocity, they give the known profiles by Rankine, Scully and Burgers respectively. The axial velocity distribution may vary in wide limits, achieved by changing the parameters of the helical symmetry. Moreover, this approach permits us to construct a composite vortex consisting of two or more cylindrical vortices. In such a manner one can approach the arbitrary distribution of a velocity field with axial symmetry.

A model of a helical vortex with a core represented by a continuous distribution of the helical vortex filaments is proposed. The velocity induced at any point of the flow is calculated by means of an integrating solution for an infinitely thin vortex filament over a corresponding part of a cross-section of the vortex (see § 5.1). As a result we obtained relatively simple formulae for both velocities averaged over an angular coordinate and the frequency of the precessing helical vortex in a tube. These calculations are in good agreement with the experimental data. Notice that the frequency of the precessing vortex in a bounded space depends not only on the self-induced velocity but also on the velocity at the channel axis and the velocity induced by a solid wall. The helical structure may rotate in any direction and even be immobile under certain conditions. This point explains the existence of stationary (immobile) helical structures in a vortex chamber.

Experimental study of the helical vortices was carried out in a vertical hydrodynamical vortex chamber with a tangential supply of liquid through turning nozzles (figure 1). Various kinds of vortex structures were formed, mainly by means of changing the boundary conditions on the chamber bottom and at the exit cross-section. The shape of the chamber cross-section, the Reynolds number and the swirl parameter had an insignificant effect on the structure of the swirl flow. A series of structures were found whose kinematics agree in general with the statements and conclusions of the theoretical model developed: a rectilinear vortex (figure 10); a composite columnar vortex (figure 17); a right-handed helical vortex (figure 28); a left-handed helical vortex (figure 27); a vortex with changing helical symmetry (figure 29); a precessing vortex (figure 21); and a double helix – two entangled vortex filaments of the same sign (figure 30). Thus the helical vortices arising in swirl flows have been classified.

This work was partially supported by a Grant from the President of the Russian Federation, by the joint foundation INTAS-RFBR Grant No. 95-IN-RU-1149 and by RFBR (Grants No. 97-05-65254 and No. 96-01-01667).

REFERENCES

Abramovich, G. N. 1951 *Applied Gas Dynamics*. Izd. Tekhn.-Teor. Lit. Moskva-Leningrad (in Russian).

Acarlar, M. S. & Smith, C. R. 1987 A study of hairpin vortices in a laminar boundary. *J. Fluid Mech.* **175**, 1–83.

Alekseenko, S. V. & Okulov, V. L. 1996 Swirl flow in technical applications (review). *Thermophysics and Aeromechanics* **3**, 97–128.

Alekseenko, S. V. & Shtork, S. I. 1992 Swirling flow large-scale structures in a combustor model. *Russian J. Engng Thermophys.* **2**, 231–266.

Alekseenko, S. V., Kuibin, P. A., Okulov, V. L. & Shtork, S. I. 1994 Characteristics of swirl flows with helical symmetry. *Tech. Phys. Lett*. **20**, 737–739.

Bandyopadhyay, P. R. & Gad-el-Hak, M. 1996 Rotating gas-liquid flows in finite cylinders: Sensitivity of standing vortices to end effects. *Exps. Fluids* **21**, 124–138.

Borissov, A. A., Kuibin, P. A. & Okulov, V. L. 1993 Flame shapes in swirl flow. *Russian J. Engng Thermophys.* **3**, 243–255.

Borissov, A. A., Kuibin, P. A. & Okulov, V. L. 1994 Calculation of Ranque effect in vortex tube. *Acta Mechanica* [Suppl.] **4**, 289–295.

Boubnov, B. M. & Golitsyn, G. S. 1986 Experimental study of convective structure in rotating fluids. *J. Fluid Mech.* **167**, 503–531.

Brücker, Ch. & Althaus, W. 1992 Study of vortex breakdown by particle tracking velocimetry (PTV). Part 1: Bubble-type vortex breakdown. *Exps. Fluids* **13**, 339–349.

Burgers, J. M. 1940 Application of a model system to illustrate some points of the statistical theory of free turbulence. *Proc. Kon. Ned. Akad. v. Wetensch* **XLIII**, 2–12.

Cassidy, J. J. & Falvey, H. T. 1970 Observation of unsteady flow arising after vortex breakdown. *J. Fluid Mech.* **41**, 727–736.

Chanaud, R. C. 1965 Observations of oscillatory motion in certain swirling flows. *J. Fluid Mech.* **21**, 111–127.

Chandrsuda, C., Mehta, R. D., Weir, A. D. & Bradshow, P. 1978 Effect of free-stream turbulence on large structure in turbulent mixing layers. *J. Fluid Mech.* **85**, 693–704.

Crow, S. C. 1970 Stability theory for a pair of trailing vortices. *AIAA J.* **8**, 2172–2179.

Dritschel, D. G. 1991 Generalized helical Beltrami flows in hydrodynamics and magnetohydrodynamics. *J. Fluid Mech.* **222**, 525–541.

Escudier, M. P. 1988 Vortex breakdown: observations and explanations. *Prog. Aerospace Sci.* **25**, 189–229.

Escudier, M. P., Bornstein, J. & Maxworthy, T. 1982 The dynamics of confined vortices. *Proc. R. Soc. Lond.* A **382**, 335–360.

Escudier, M. P., Bornstein, J. & Zehnder, N. 1980 Observations and LDA measurements of confined turbulent vortex flow. *J. Fluid Mech.* **98**, 49–63.

Faler, J. H. & Leibovich, S. 1977 Disrupted states of vortex flow and vortex breakdown. *Phys. Fluids* **20**, 1385–1400.

Feikema, D., Chen, R.-H. & Driscoll, J. F. 1990 Enchancement of flame blow-out limits by the use of swirl. *Combust. Flame* **80**, 183–195.

Fukumoto, Y. & Miyazaki, T. 1991 Three-dimensional distortions of a vortex filament with axial velocity. *J. Fluid Mech.* **222**, 369–416.

Garg, A. K. & Leibovich, S. 1979 Spectral characteristics of vortex breakdown flowfields. *Phys. Fluids* **22**, 2053–2064.

Goldshtick, M. A. 1981 *Vortex Flows*. Novosibirsk, Nauka (in Russian).

Guarga, R. F., Gracia, J. S., Sanchez, A. H. & Rodal, E. C. 1985 LDV and pressure measurements in swirling confined, turbulent and non-cavitating flows. In *Work Group on the Behaviour of Hydraulic Machinery Under Steady Oscillatory Conditions, Paper* 12.

Gupta, A. K., Lilley, D. G. & Syred, N. 1984 *Swirl Flows*. Abacus Press.

Hardin, J. S. 1982 The velocity field induced by a helical vortex filament. *Phys. Fluids* **25**, 1949–1952.

Hashimoto, H. 1971 Theoretical study of swirling flow accompanied by helical cavity core in circular pipe. *Rep. Inst. High Speed Mech.* **23**, No 228, 61–97.

Hopfinger, E. J. & Heijst, G. J. F. van 1993 Vortices in rotating fluids. *Ann. Rev. Fluid Mech.* **25**, 241–289.

Ishizuka, S. 1989 An experimental study on extinction and stability of tubular flames. *Combust. Flame* **75**, 367–379.

Joukowski, N. E. 1912 Vortex theory of a rowing helical. *Trudy Otdeleniya Fizicheskikh Nauk Obshchestva Lubitelei Estestvoznaniya* **16**, 1–31 (in Russian).

Kelvin, Lord 1880 Vibrations of a columnar vortex. *Phil. Mag.* **10**, 155–168.

Kida, S. 1981 A vortex filament moving without change of form. *J. Fluid Mech.* **112**, 397–409.

Kuibin, P. A. & Okulov, V. L. 1994 Determination of frequency of helical vortex precession. *Tech. Phys. Lett.* **20**, 274–275.

Kuibin, P. A. & Okulov, V. L. 1998 Self-induced motion and asymptotic expansion of the velocity field in the vicinity of a helical vortex filament. *Phys. Fluids* **10**, 607–614.

Kumar, R. & Conover, T. 1993 Flow visualization studies of a swirling flow in a cylinder. *Expl Therm. Fluid Sci.* **7**, 254–262.

Kutateladze, S. S., Volchkov, E. P. & Terekhov, V. I. 1987 *Aerodynamics, Heat and Mass Transfer in Confined Vortex Flows.* Institute of Thermophysics, Novosibirsk (in Russian).

Landman, M. J. 1990 On the generation of helical waves in circular pipe flow. *Phys. Fluids* A **2**, 738–747.

Lamb, H. 1932 *Hydrodynamics*, 6th edn. Cambridge University Press.

Leibovich, S. 1978 The structure of vortex breakdown. *Ann. Rev. Fluid Mech.* **10**, 221–246.

Leibovich, S. 1984 Vortex stability and breakdown: survey and extension. *AIAA J.* **22**, 1192–1206.

Lessen, M., Singh, P. J. & Paillet, F. 1974 The stability of a trailing line vortex. Part 1. Inviscid theory. *J. Fluid Mech.* **63**, 753–763.

Levy, H. & Forsdyke, A. G. 1928 The steady motion and stability of a helical vortex. *Proc. R. Soc. Lond.* A **120**, 670–690.

Maxworthy, T., Hopfinger, E. J. & Redekopp, L. G. 1985 Wave motion on vortex cores. *J. Fluid Mech.* **151**, 141–165.

Mollenkopf, G. & Raabe, J. 1970 Measurements of velocity and pressure in the draft tube of a Francis turbine. *B3.* Presented at *5th IAHR-Symposium, Stockholm, Sweden.*

Moore, D. W. & Saffman, P. G. 1972 The motion of a vortex filament with axial flow. *Phil. Trans. R. Soc. Lond.* A **272**, 403–429.

Okulov, V. L. 1993 Resonance hydro-acoustic processes in the channels of machines and units with intensive swirling of flows. Doctoral dissertation, Institute of Thermophysics, Novosibirsk (in Russian).

Okulov, V. L. 1995 The velocity field induced by vortex filaments with cylindrical and conic supporting surface. *Russian J. Engng Thermophys.* **5**, 63–75.

Ovchinnikov, A. A. & Nikolaev, N. A. 1973 Determination of the vortex radius in gas vortex chambers. *Trudy Kazanskogo Khimiko-Tekhnologicheskogo Instituta* **1**, 9–14 (in Russian).

Perry, A. E. & Lim, T. T. 1978 Coherent structures in coflowing jets and wakes. *J. Fluid Mech.* **88**, 451–463.

Ricca, R. L. 1994 The effect of torsion on the motion of a helical vortex filament. *J. Fluid Mech.* **273**, 241–259.

Saffman, P. G. 1992 *Vortex Dynamics.* Cambridge University Press.

Sarpkaya, T. 1971 On stationary and travelling vortex breakdown. *J. Fluid Mech.* **45**, 545–559.

Scully, M. P. 1975 Computation of helicopter rotor wake geometry and its influence on rotor harmonic airloads. *Massachusetts Inst. of Technology Pub.* ARSL TR 178-1. Cambridge.

Shtork, S. I. 1994 Experimental investigation of vortex structures in tangential chambers. Candidate dissertation, Institute of Thermophysics, Novosibirsk (in Russian).

Shtym, A. N. 1985 *Aerodynamics of Cyclone-Vortex Chambers.* Far-Eastern University, Vladivostok (in Russian).

Sozou, C. J. & Swithenbank, J. 1969 Adiabatic transverse waves in a rotary fluid. *J. Fluid Mech.* **38**, 657–671.

Takaki, R. & Hussain, A. K. M. F. 1984 Dynamics of entangled vortex filaments. *Phys. Fluids* **27**, 761–763.

Widnall, S. E. 1972 The stability of helical vortex filament. *J. Fluid Mech.* **54**, 641–663.

Widnall, S. E. & Bliss, D. B. 1971 Slender-body analysis of the motion and stability of a vortex filament containing an axial flow. *J. Fluid Mech.* **50**, 335–353.

Yazdabadi, P. A., Griffiths, A. J. & Syred, N. 1994 Characterization of the PVC phenomena in the exhaust of cyclone dust separator. *Exps. Fluids* **17**, 84–95.